Some DEEPWAVE Activities @ DLR

Andreas Dörnbrack et al.

DLR Oberpfaffenhofen

Institut für Physik der Atmosphäre

Sonja‘s Met Paper

What do we see in ground-based lidar data?

ECMWF Temperature vs Lidar Temperature

DEEPWAVE Meeting, NRL Monterey, 10 December 2016

List of Publications (DEEPWAVE)

Gisinger, S., A. Dörnbrack, V. Matthias, J. D. Doyle, S. D. Eckermann, B. Ehard, L. Hoffmann, B. Kaifler, C. G. Kruse, and M. Rapp, 2016: Atmospheric Conditions during the Deep Propagating Gravity Wave Experiment (DEEPWAVE), *Mon. Wea. Rev.* , submitted 16 November 2016

Kaifler, N., Kaifler, B., Ehard, B., Gisinger, S., Dörnbrack, A., Rapp, M.,Kivi, R., Kozlovsky, A., Lester, M., and Liley, B., 2016: Observational evidence of downward-propagating gravity waves in middle atmospheric lidar data, *Journal of Atmospheric and Solar-Terrestrial Physics*, submitted 5 November 2016

Ehard, B., B. Kaifler, A. Dörnbrack, P. Preusse, S. D. Eckermann, M. Bramberger, S. Gisinger, N. Kaifler, B. Liley, J. Wagner, and M. Rapp, 2016: Vertical propagation of large amplitude mountain waves in the vicinity of the polar night jet, *J. Geophys. Res.*, submitted 6 July 2016, resubmitted 7 November 2016

Kaifler, B., N. Kaifler, B. Ehard, A. Dörnbrack, M. Rapp, and D. C. Fritts, 2015: Influences of source conditions on mountain wave penetration into the stratosphere and mesosphere, *Geophys. Res. Lett.,* 42, doi:10.1002/2015GL066465.

Dörnbrack, A., S. Gisinger, and B. Kaifler, 2016: On the interpretation of gravity wave measurements by ground-based lidars, *Atmosphere,* submitted 2 December 2016

To be submitted January 2017:

Portele, T. C., A. Dörnbrack, B. & N. Kaifler, J. S. Wagner, P.-D. Pautet, and M. Rapp, 2017: Mountain Wave Propagation under Transient Tropospheric Forcing: A DEEPWAVE Case Study. *Mon. Wea. Rev.*, to be submitted 2017

List of Publications (GW-LCYCLE I and II)

Wagner, J., Dörnbrack, A., Rapp, M., Gisinger, S., Ehard, B., Bramberger, M., Witschas, B., Chouza, F., Rahm, S., Mallaun, C., Baumgarten, G., and Hoor, P., 2016: Observed versus simulated mountain waves over Scandinavia – improvement by enhanced model resolution? *Atmos. Chem. Phys. Discuss.*, doi:10.5194/acp-2016-765, in review, 2016.

Dörnbrack, A., S. Gisinger, M. C. Pitts, L. R. Poole, and M. Maturilli, 2016: Multilevel cloud structure over Svalbard, *Mon. Wea. Rev.* , DOI: http://dx.doi.org/10.1175/MWR-D-16-0214.1

Matthias, V., A. Dörnbrack, and G. Stober, 2016: The extraordinarily strong and cold polar vortex in the early northern winter 2015/16, *Geophys. Res. Lett.,* **43**, doi:10.1002/2016GL071676.

Atmospheric Conditions during the Deep Propagating Gravity Wave Experiment (DEEPWAVE)

Sonja Gisinger[1], Andreas Dörnbrack[1], Vivien Matthias[2], James D. Doyle[3], Stephen D. Eckermann[4], Benedikt Ehard[1], Lars Hoffmann[5], Bernd Kaifler[1], Christopher G. Kruse[6] and Markus Rapp[1, 7]

Paper Submitted to Mon. Wea. Rev., 16 November 2016

1 Deutsches Zentrum für Luft- und Raumfahrt, Institut für Physik der Atmosphäre, Oberpfaffenhofen, Germany

2 Leibniz Institute of Atmospheric Physics at the University of Rostock, Kühlungsborn, Germany

3 Marine Meteorology Division, U.S. Naval Research Laboratory, Monterey, California, USA

4 Space Science Division, U.S. Naval Research Laboratory, Washington, D. C., USA

5 Jülich Supercomputing Centre, Forschungszentrum Jülich, Jülich, Germany

6 Department of Geology and Geophysics, Yale University, USA

7 Meteorologisches Institut München, Ludwig-Maximilian-Universität München, Germany

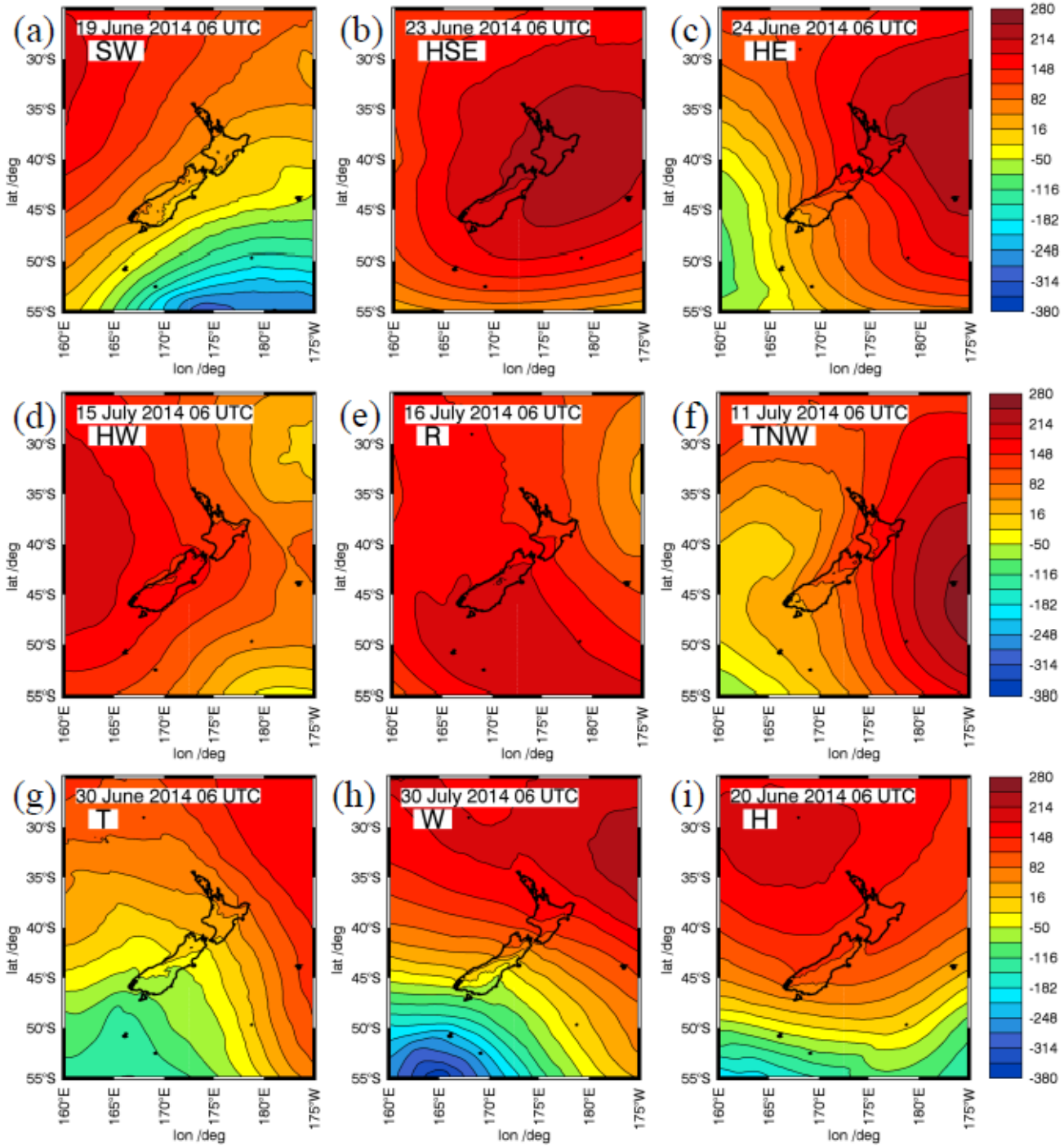
(a)
19 June 2014 06 UTC
SW
(b)
23 June 2014 06 UTC
HSE
(c)
24 June 2014 06 UTC
HE
(d)
15 July 2014 06 UTC
HW
(e)
16 July 2014 06 UTC
R
(f)
11 July 2014 06 UTC
TNW
(g)
30 June 2014 06 UTC
T
(h)
30 July 2014 06 UTC
W
(i)
20 June 2014 06 UTC
H
lat /deg
30°S
35°S
40°S
45°S
50°S
55°S
lon /deg
160°E
165°E
170°E
175°E
180°E
175°W
280
214
148
82
16
-50
-116
-182
-248
-314
-380

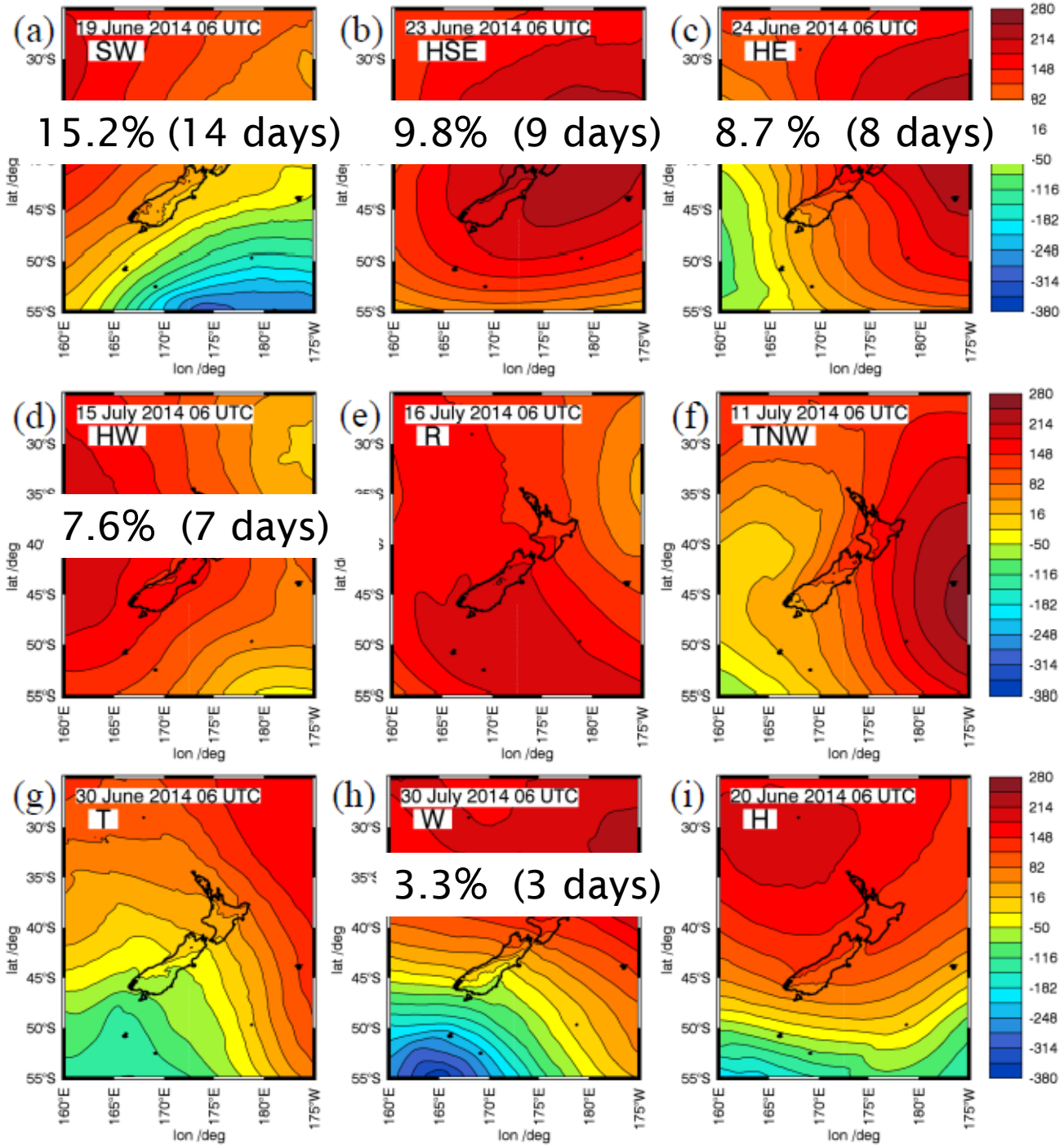
(a)
19 June 2014 06 UTC
SW
(b)
23 June 2014 06 UTC
HSE
(c)
24 June 2014 06 UTC
HE
15.2% (14 days)
9.8% (9 days)
8.7 % (8 days)
(d)
15 July 2014 06 UTC
HW
(e)
16 July 2014 06 UTC
R
(f)
11 July 2014 06 UTC
TNW
7.6% (7 days)
(g)
30 June 2014 06 UTC
T
(h)
30 July 2014 06 UTC
W
3.3% (3 days)
(i)
20 June 2014 06 UTC
H
lat /deg
lon /deg
280
214
148
82
16
-50
-116
-182
-248
-314
-380

IOP	RF	FF	Date	Target	Weather regime
1	01		June 6	MW/TW/PF SI	HE
3	04		June 14	MWs/TWs SI	HE
4	05		June 16	MWs/TWs SI	TNW
6	07		June 19	MWs/CWs/FWs E. Ocean	SW
7	08		June 20	MWs/TWs SI	H
8	09 10		June 24 June 25	MWs SI MWs/TWs SI	HE TNW
9	12 13 14	 01/02 	June 29 June 30 July 1	MWs/TWs SI MWs SI MWs/TWs SI	TNW T T
10	16	04/05	July 4	MWs/TWs SI	SW
13	20 21 22	06 07/08 09 10	July 10 July 11 July 12 July 13	PF/MW SO SI MWs SI MWs SI MWs SI	TNW TNW TNW TSW
15		12	July16	MWs SI	R
16	26		July 20	MWs SI along mountain ridge	SW

Table 1: Assigned weather regimes of DEEPWAVE IOPs focusing on mountain and trailing waves around the South Island of New Zealand. The acronyms follow definitions in Appendix 3 of Fritts et al. (2016). Compare also Table 4 of Fritts et al. (2016) for summaries of the research flights of the NSF/NCAR GV (RF) and the DLR Falcon (FF).

V_H /m s^{-1}

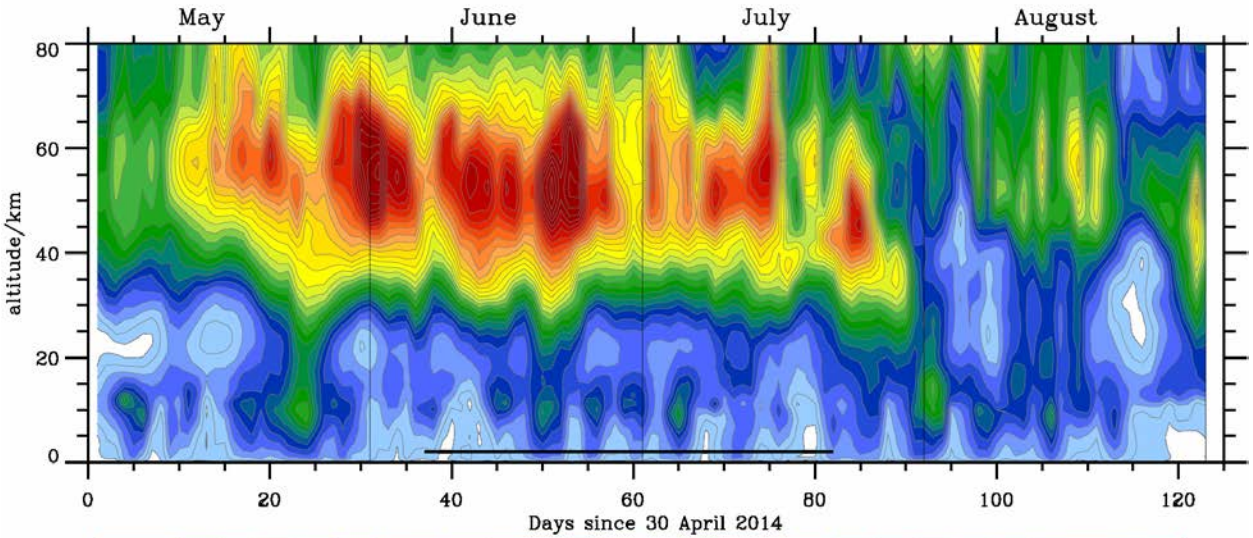

α_H / °

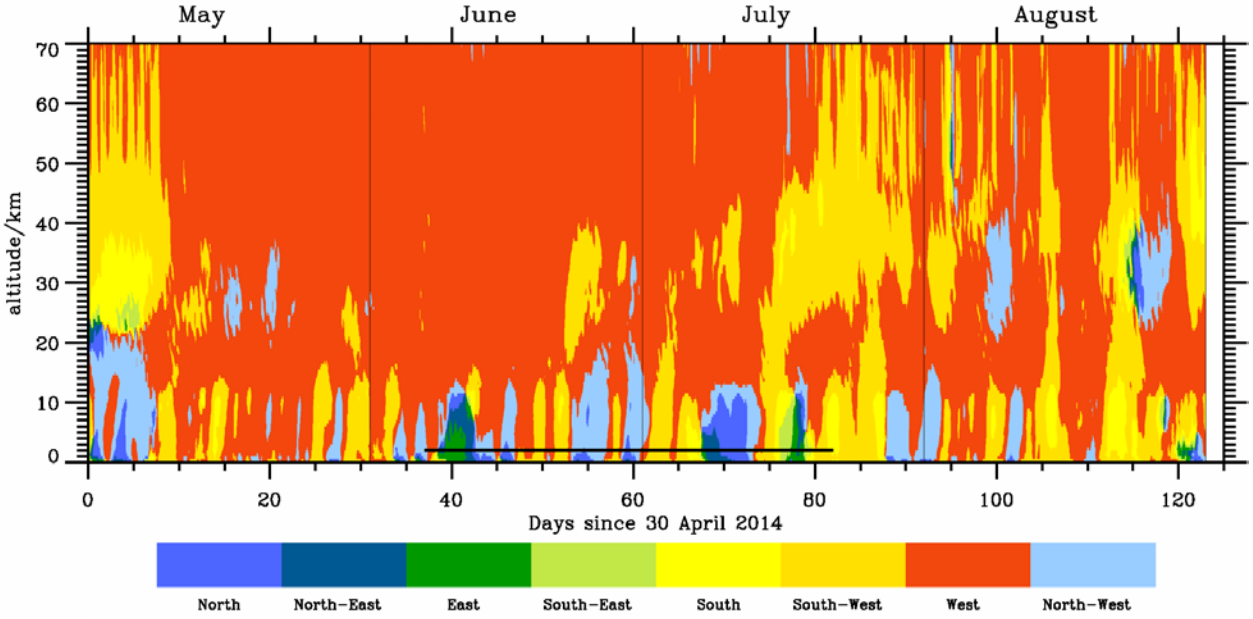

Vertical time series of ECMWF T_L1279/L137 operational analyses averaged over the area between 40°S to 50°S and 165°E to 180°E

Tropopause Inversion Layer

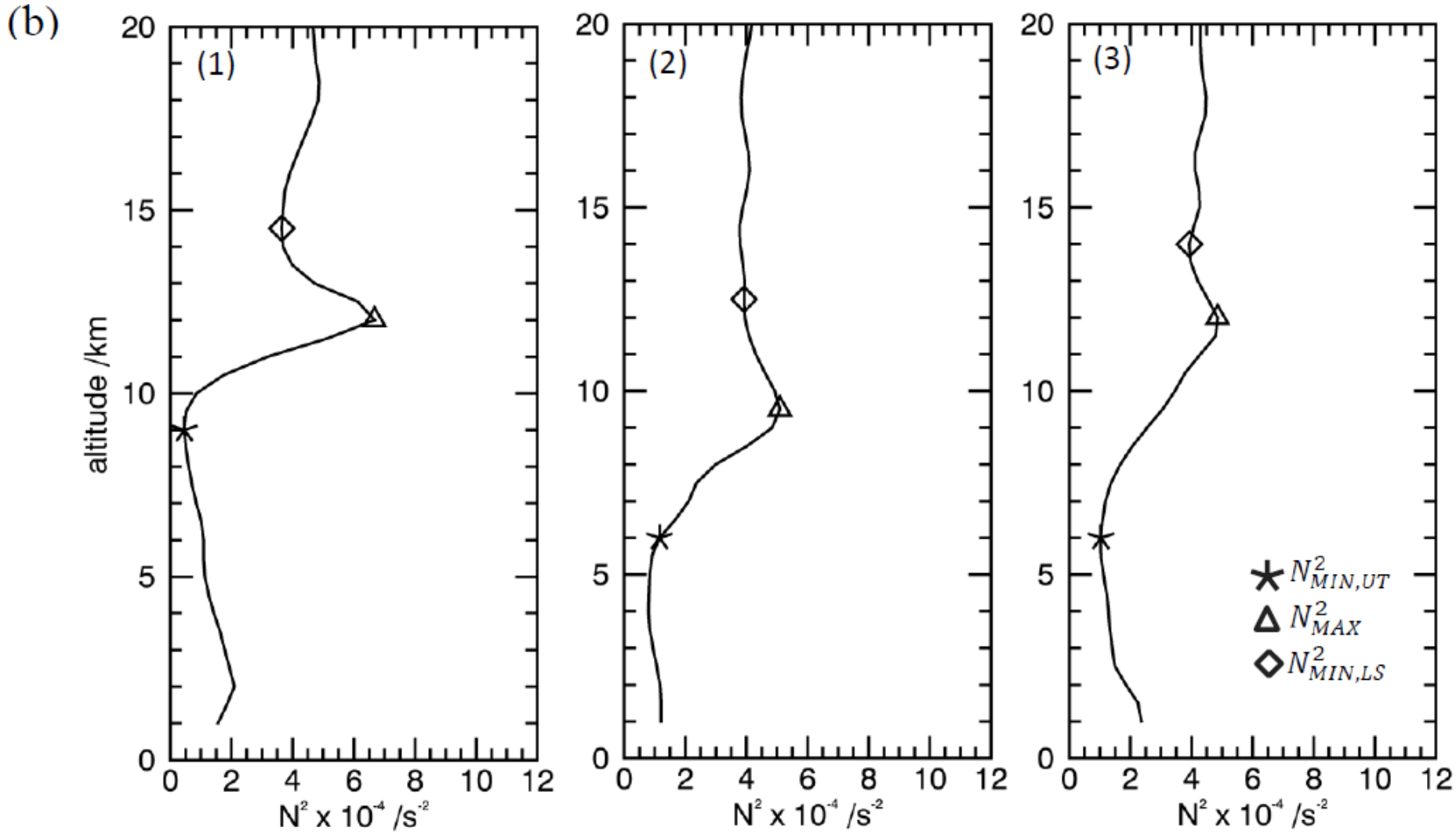

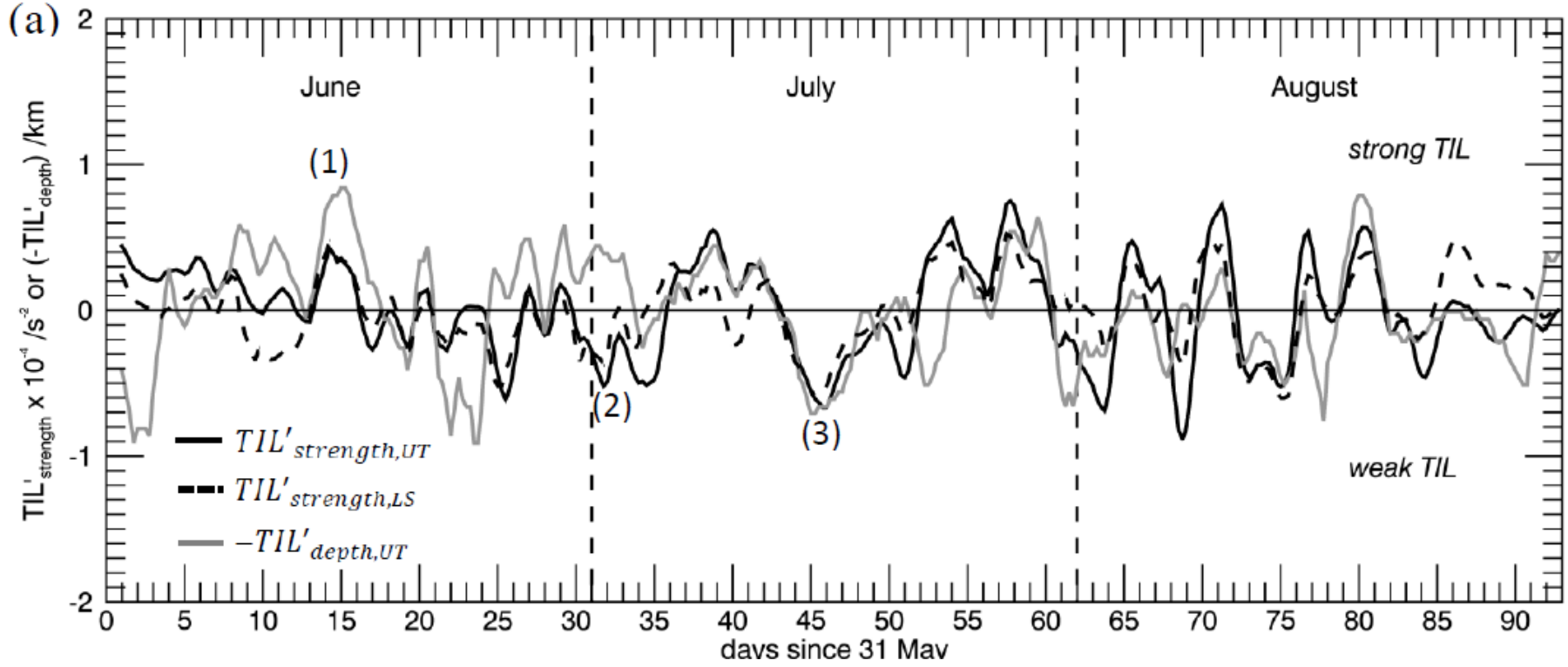

$$(2)\ TIL'_{strength,UT} = \frac{1}{2}\left(N^2_{MAX} - N^2_{MIN,UT}\right) - \underbrace{\left\langle \frac{1}{2}\left(N^2_{MAX} - N^2_{MIN,UT}\right)\right\rangle_{JJA}}_{\text{mean } TIL_{strength,UT}}$$

$$(3)\ TIL'_{strength,LS} = \frac{1}{2}\left(N^2_{MAX} - N^2_{MIN,LS}\right) - \underbrace{\left\langle \frac{1}{2}\left(N^2_{MAX} - N^2_{MIN,LS}\right)\right\rangle_{JJA}}_{\text{mean } TIL_{strength,LS}},$$

$$(4)\ TIL'_{depth,UT} = \frac{1}{2}\left[h(N^2_{MAX}) - h(N^2_{MIN,UT})\right] - \underbrace{\left\langle \frac{1}{2}\left[h(N^2_{MAX}) - h(N^2_{MIN,UT})\right]\right\rangle_{JJA}}_{\text{mean } TIL_{depth,UT}},$$

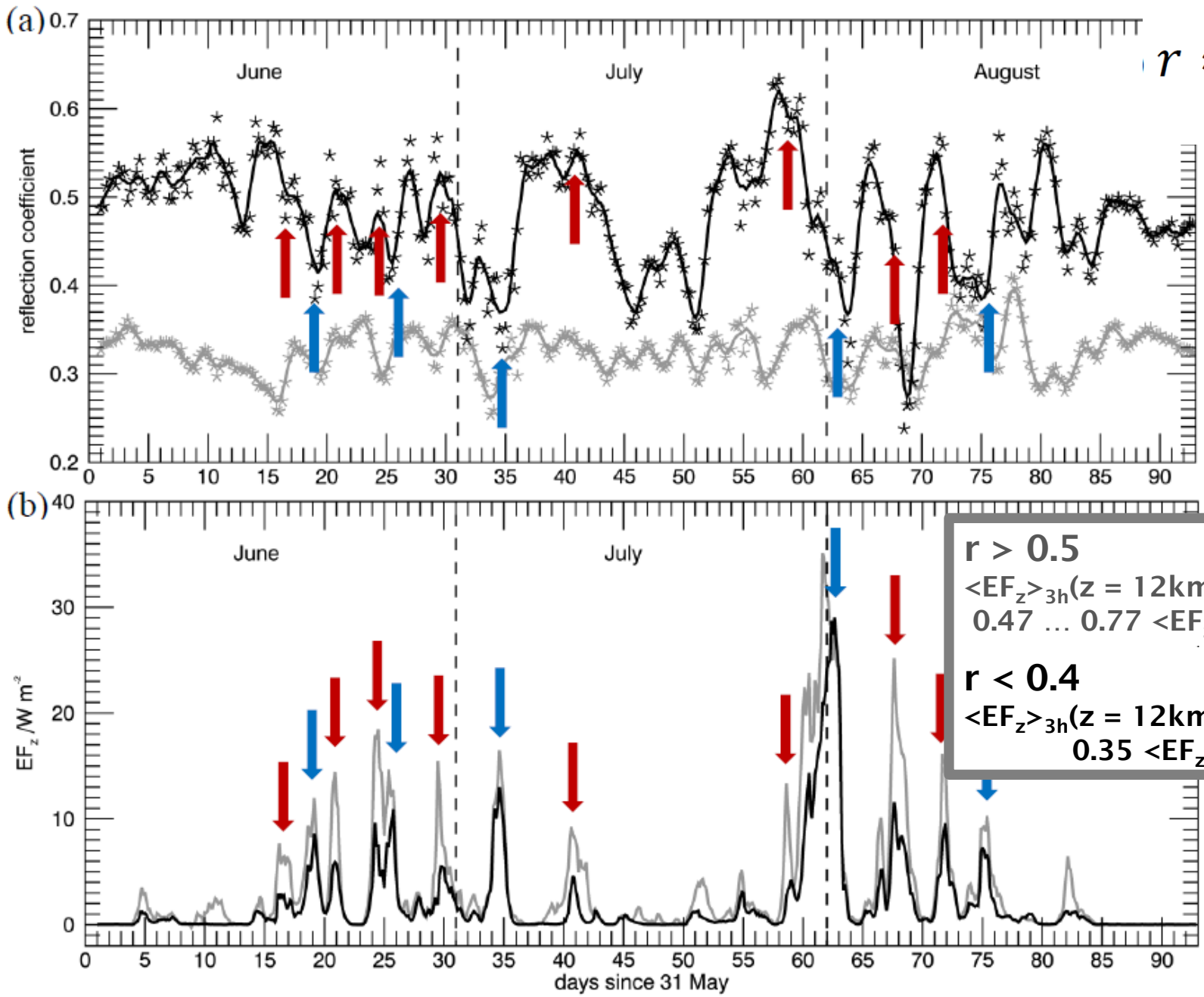
(a)
June
July
August
reflection coefficient
(b)
June
July
EF$_z$ /W m^{-2}
days since 31 May
$r \approx \frac{N_S - N_T}{N_T + N_S}$,
N_S^{MAX}
<N_S>
r > 0.5
<EF$_z$>$_{3h}$(z = 12km) ~
0.47 … 0.77 <EF$_z$>$_{3h}$(z = 4km)
r < 0.4
<EF$_z$>$_{3h}$(z = 12km) <
0.35 <EF$_z$>$_{3h}$(z = 4km)
<EF$_z$>$_{3h}$(z = 12km)
<EF$_z$>$_{3h}$(z =4 km)

NZ between Subtropical Jet and Polar Front Jet

(diagnostics based on 200 hPa data at 06 UTC)

zonal averages

169° E

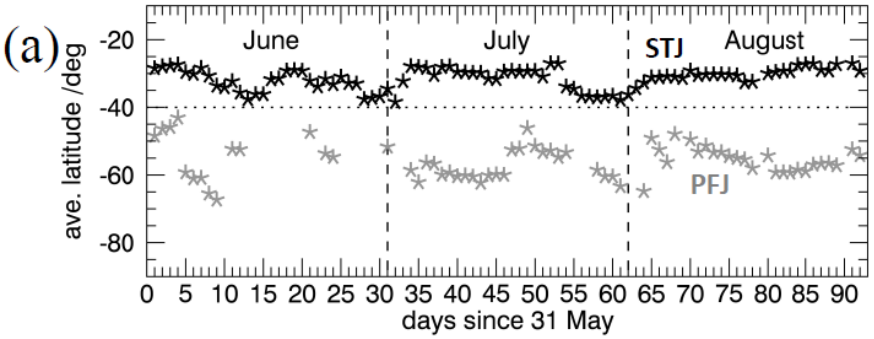

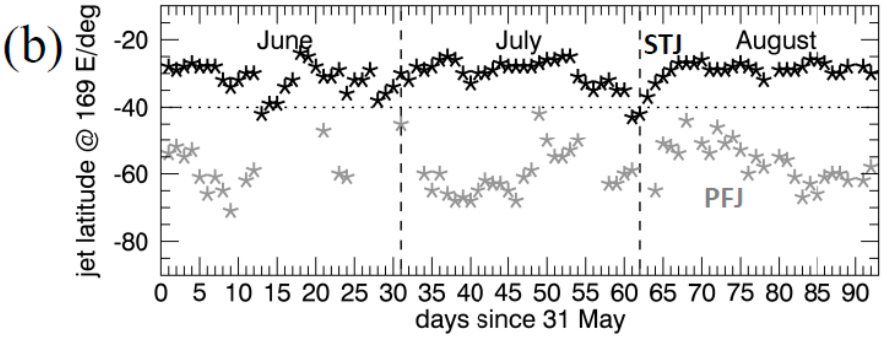

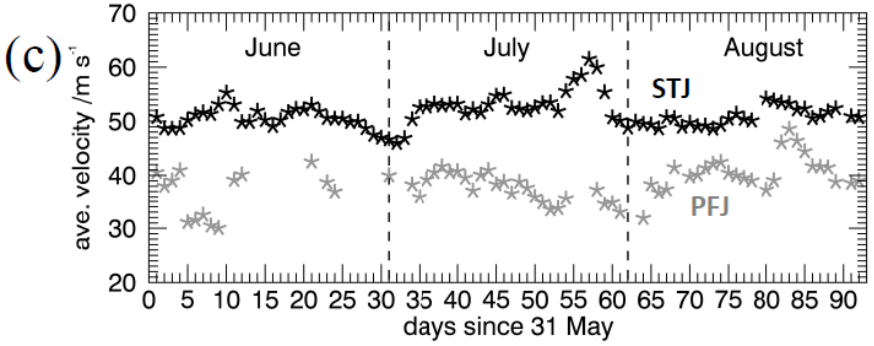

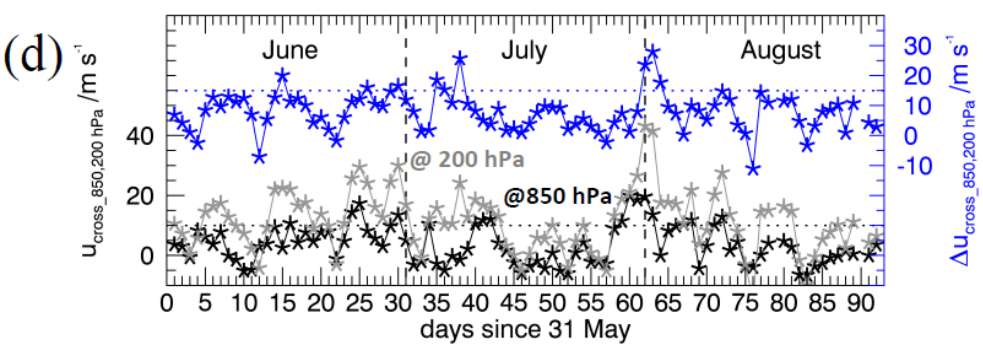

cross-mountain flow and vertical shear

NZ between Subtropical Jet and Polar Front Jet

(diagnostics based on 200 hPa data at 06 UTC)

Whenever the STJ was located close to the SI, mountain waves and sometimes even jet-stream-induced gravity waves were observed at flight level, in the stratosphere and the MLT. Additionally, wave breaking and turbulence at flight level were reported for these events.

For the cases when the PFJ was located close to the SI, weak mountain wave activity at flight level was reported. Yet, surprisingly strong mountain wave activity in the stratosphere and the MLT were also reported.

This suggests that the presence of the STJ was associated with stronger forcing conditions and larger vertical shear.

cross-mountain flow and

vertical shear

Planetary Wave Activity

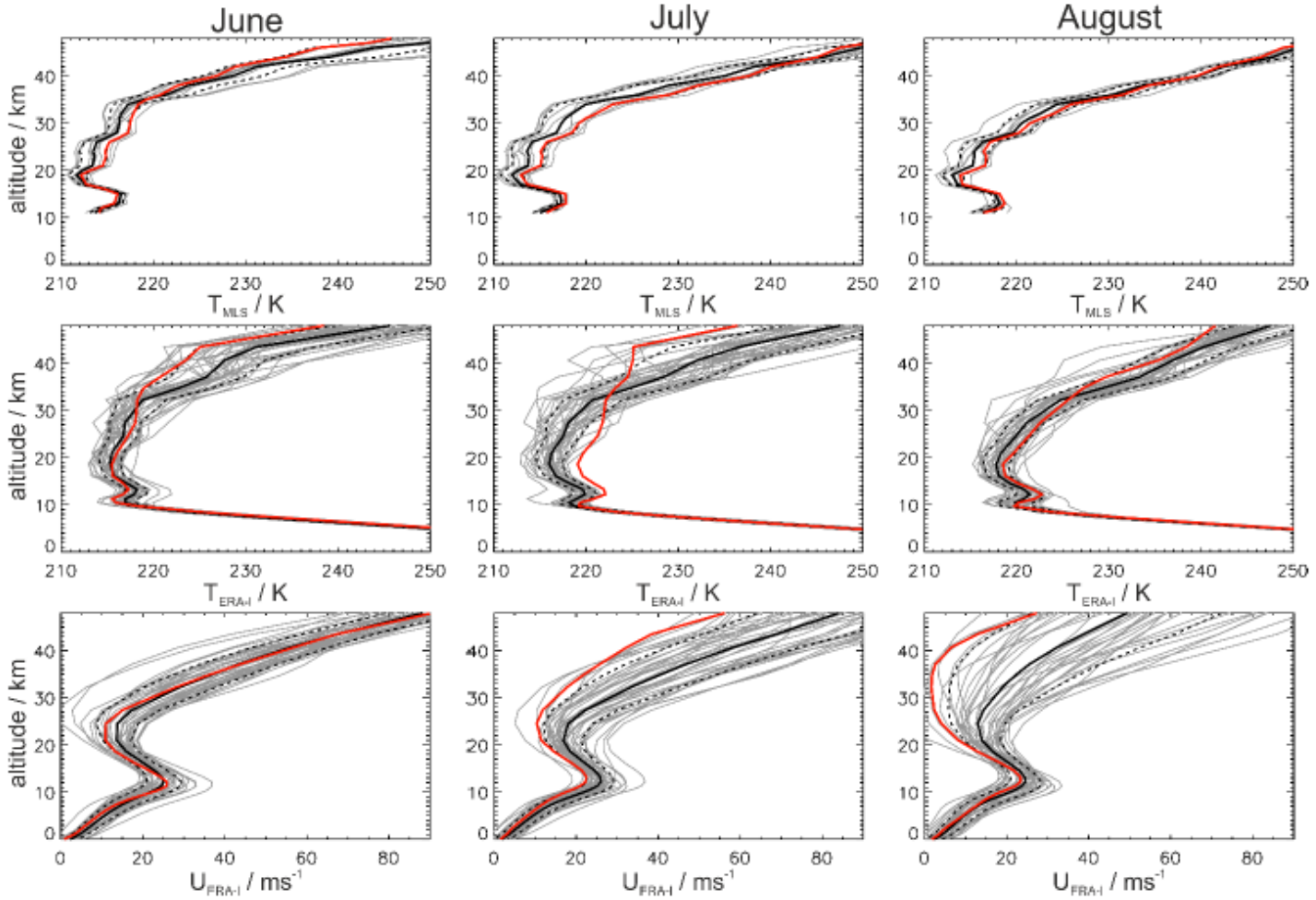

Fig. 9: Vertical profiles of the monthly-means and zonal-mean MLS temperatures T_{MLS} (top row), ERA temperatures $T_{ERA\text{-}I}$ (middle row) and ERA zonal winds (bottom row) averaged around New Zealand (35-45°S, 160-180°E). Thin grey lines represent the means from all available years (MLS = 12, ERA-Interim = 37). Solid black lines are the long-term averages and their respective standard deviations are plotted by dashed lines. The red lines represent the means for the DEEPWAVE year 2014.

Planetary Wave Activity

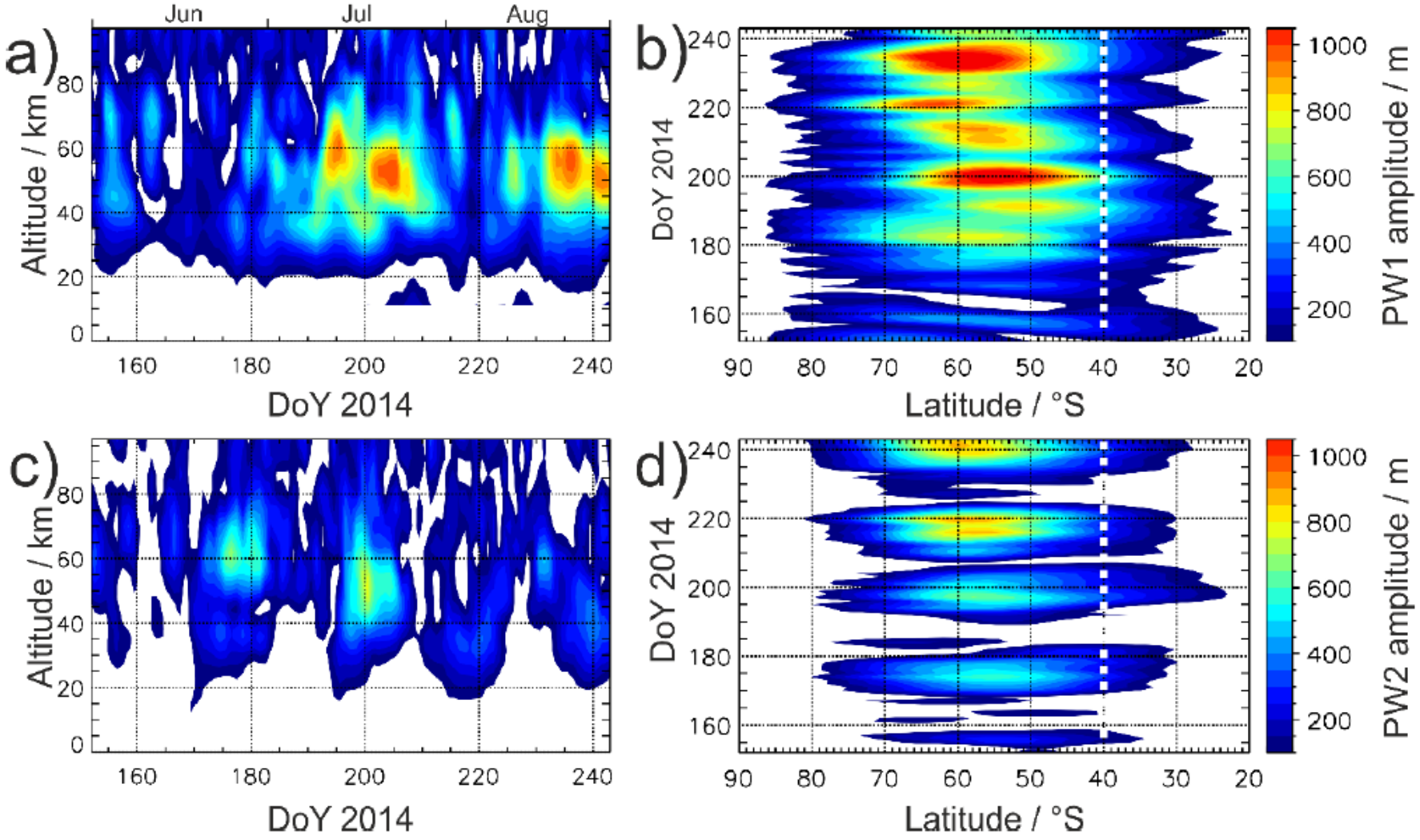

Fig. 11: Geopotential-height amplitudes of the stationary planetary waves 1 (a, b) and 2 (c, d) as function of height and time averaged between 35° S and 45°S (left column), and as function of latitude and time averaged between 30 and 40 km altitude (right column).

Hoffmann's AIRS Climatology for NZ

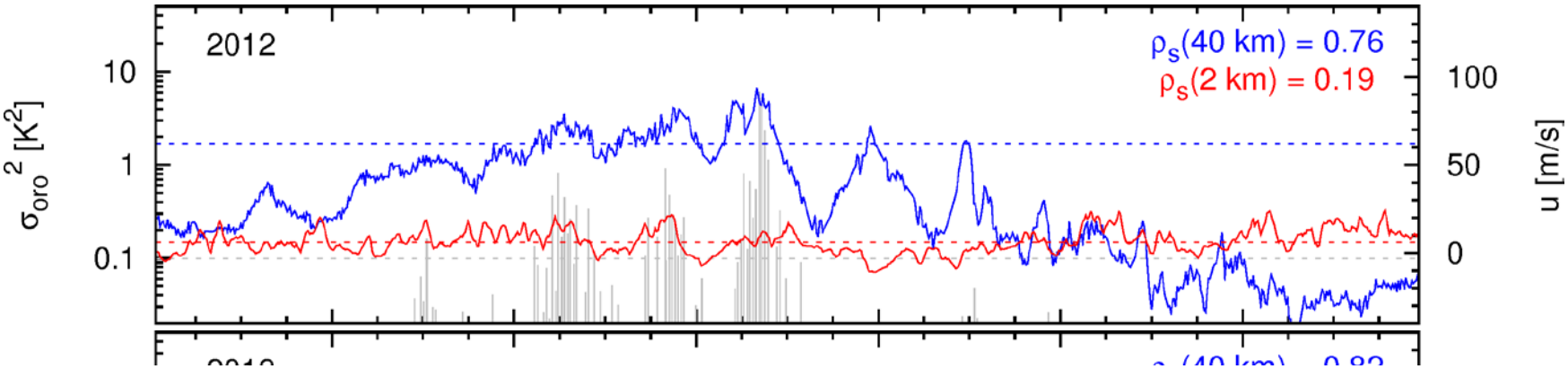

Fig. 14: Time series of AIRS 4.3 µm brightness temperature variance differences (gray) and ERA-Interim zonal winds at 2 km (red) and 40 km (blue) log-pressure altitude from 1 April to 31 October in 2012 (top), 2013 (middle), and 2014 (bottom) at New Zealand. Gray dotted lines indicate the 0.1 K^2 threshold used to detect orographic gravity waves. The red and blue dotted lines depict zonal wind levels of 6 and 64 m s^{-1} used to predict mountain wave events in the AIRS observations. The values of u are area averages for 166.5 to 176.5°E and 48 to 40°S and refer to the AIRS observational level (3 hPa, about 40 km) and the low-level (750 hPa, about 2 km).

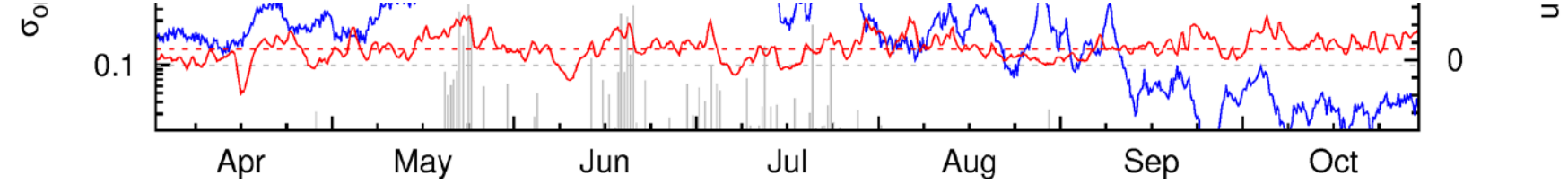

Hoffmann's AIRS Climatology

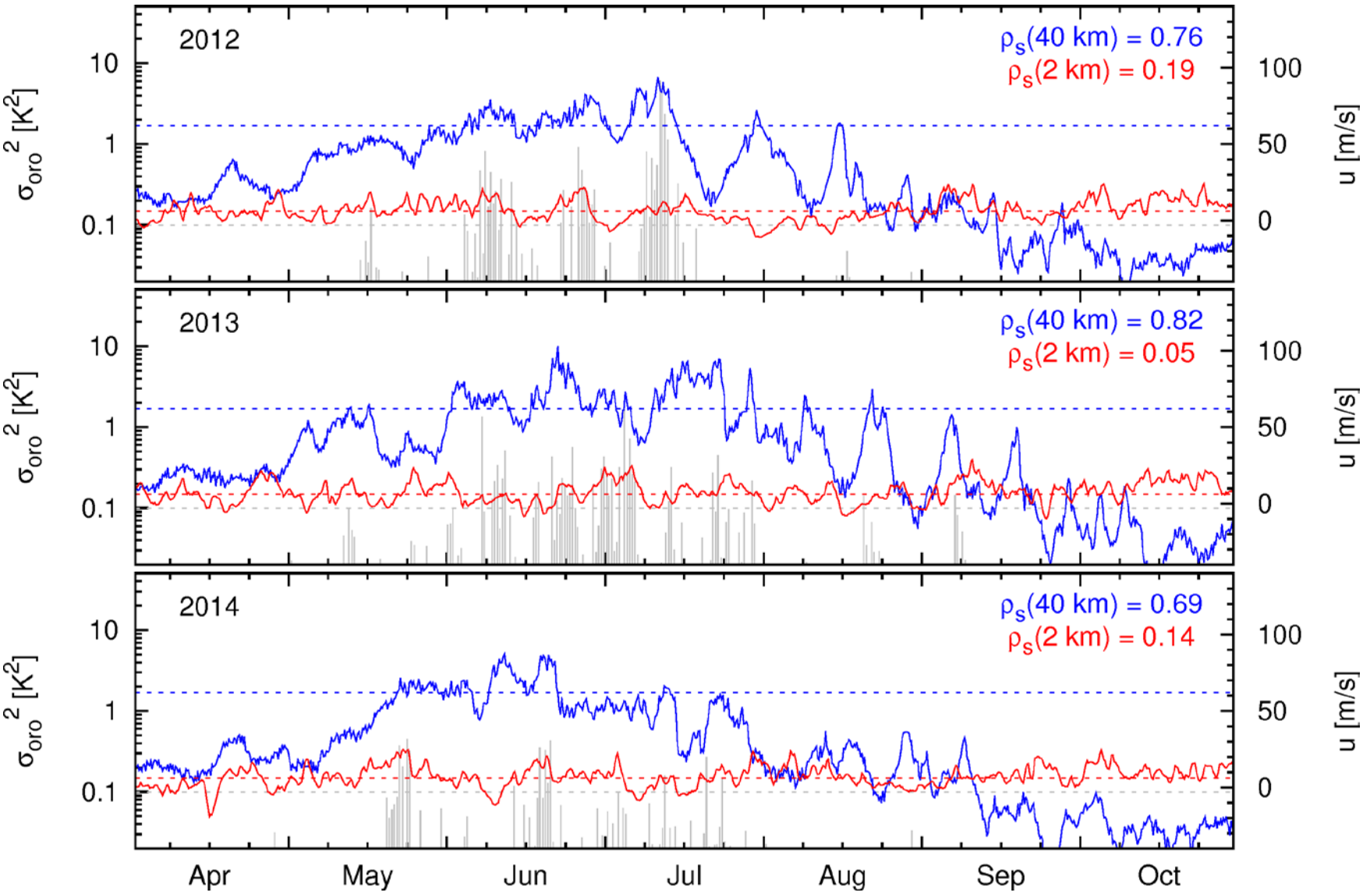

Yearly variability of inferred orographic wave activity over NZ during June/July

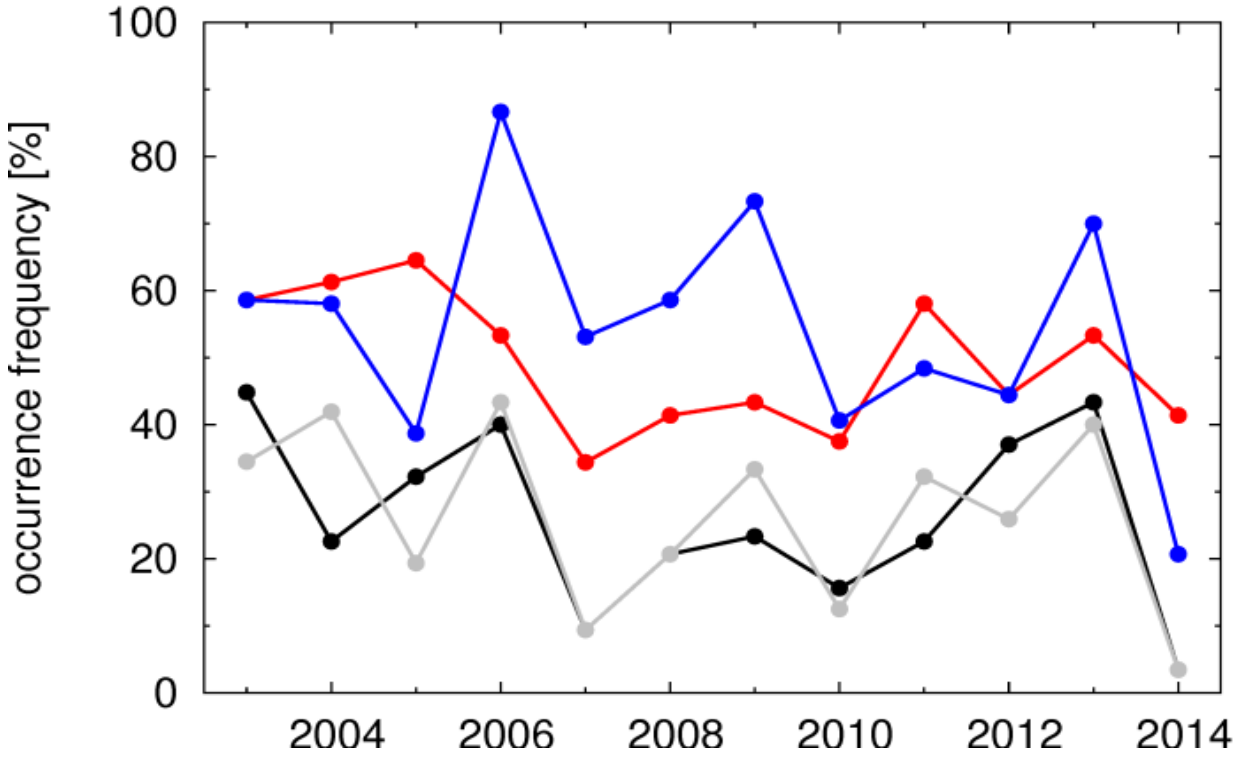

AIRS observations

simple mountain wave prediction model

zonal winds > 6 m s^{-1} at 2 km (red)

zonal winds > 64 m s^{-1} at 40 km (blue)

Steve's NAVGEM Analysis

(a)

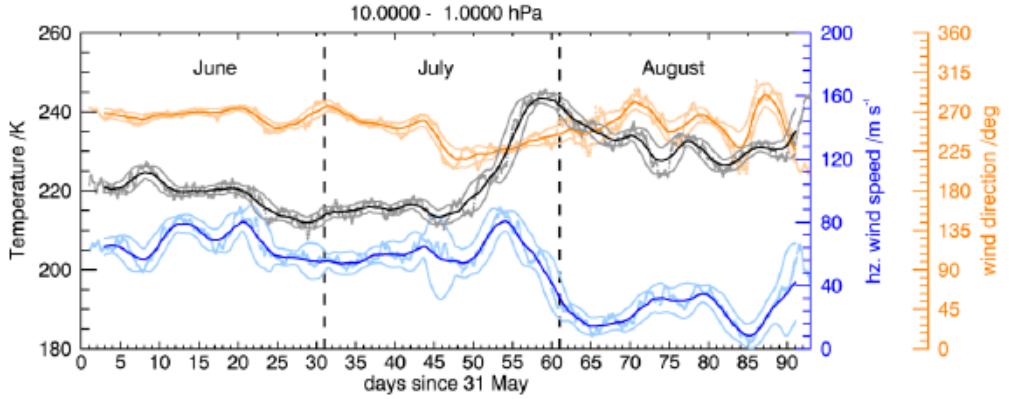

(b)

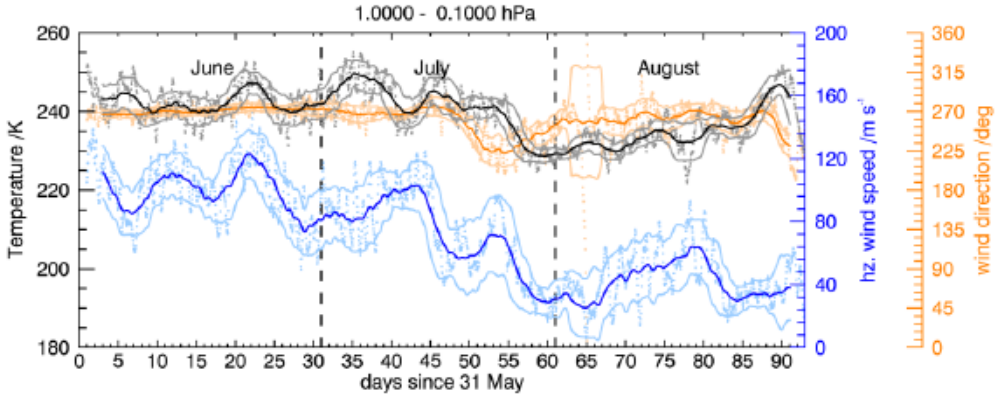

(c)

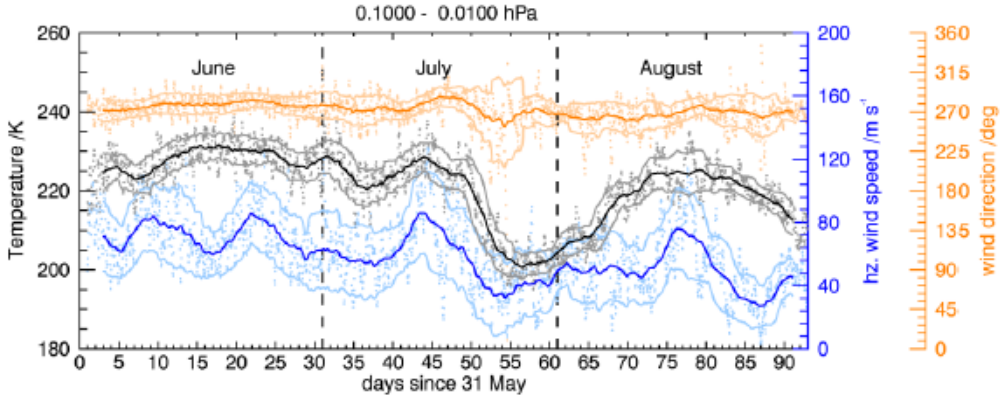

Article

On the interpretation of gravity wave measurements by ground-based lidars

Andreas Dörnbrack [1]*, Sonja Gisinger [1], and Bernd Kaifler [1]

[1] Institut für Physik der Atmosphäre, DLR Oberpfaffenhofen, Germany
* Correspondence: andreas.doernbrack@dlr.de; Tel.: +49-8153-282588

Academic Editor: name
Version December 1, 2016 submitted to Atmosphere; Typeset by LaTeX using class file mdpi.cls

Abstract: This paper asks the simple question: How can we interpret vertical time series of middle atmosphere gravity wave measurements by ground-based temperature lidars? Linear wave theory is used to show that the association of identified phase lines with quasi-monochromatic waves should be considered with great care. The ambient mean wind has a substantial effect on the inclination of the detected phase lines. The lack of knowledge about the wind might lead to a misinterpretation of the vertical propagation direction of the observed gravity waves. In addition, numerical simulations of three archetypal atmospheric mountain wave regimes show a sensitivity of virtual lidar observations on the position relative to the mountain and on the scale of the mountain.

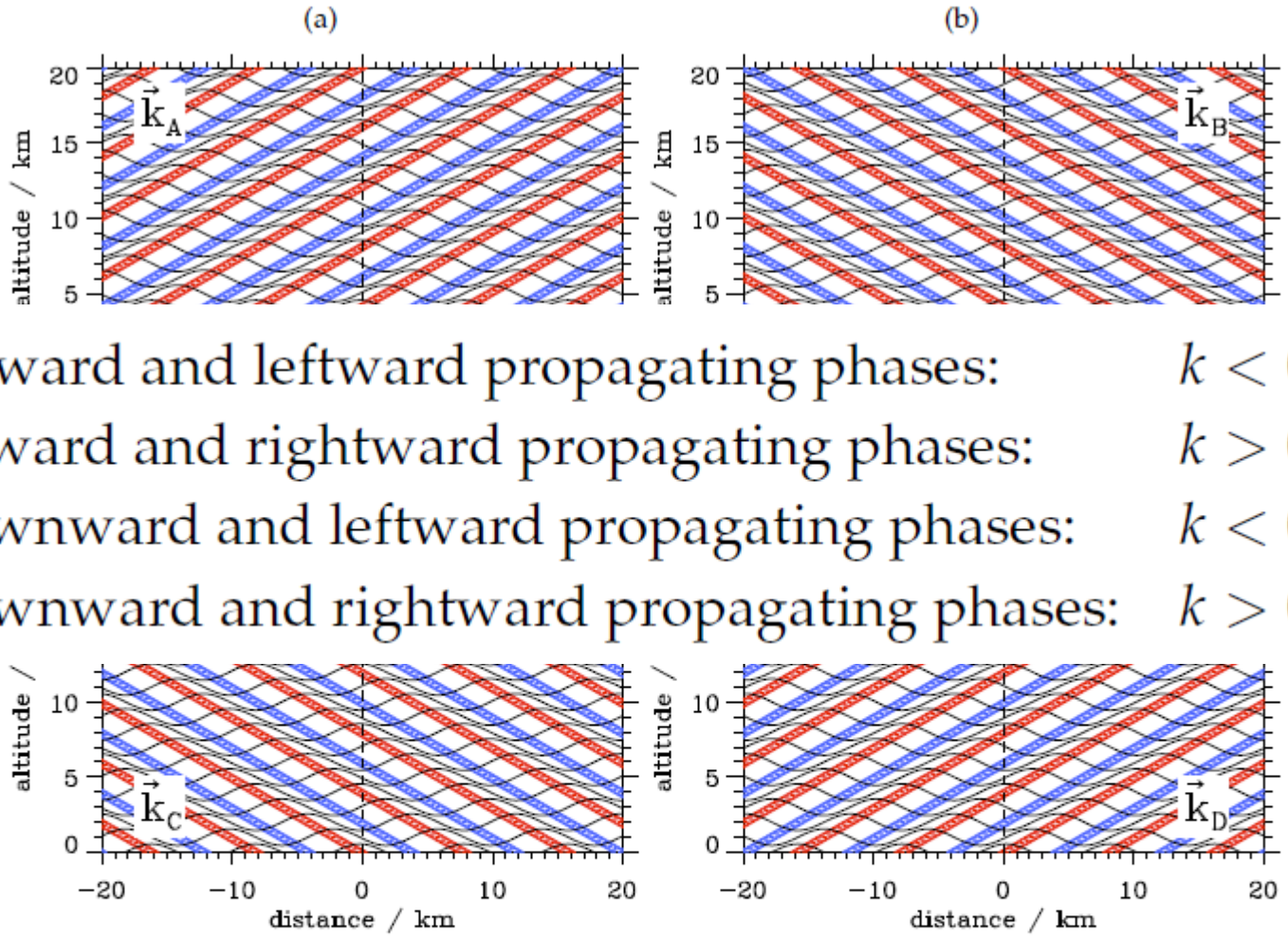

$\vec{k}_A$ upward and leftward propagating phases: $k < 0, m > 0$

$\vec{k}_B$ upward and rightward propagating phases: $k > 0, m > 0$

$\vec{k}_C$ downward and leftward propagating phases: $k < 0, m < 0$

$\vec{k}_D$ downward and rightward propagating phases: $k > 0, m < 0$

Figure 3. Spatial snapshots of the vertical displacements $\xi(x,z,t)$ of horizontally and vertically propagating plane waves for the four wavenumber vectors $\vec{k}_A$ (a), $\vec{k}_B$ (b), $\vec{k}_C$ (c), and $\vec{k}_D$ (d) at $t = 24$ min, respectively. The values of the horizontal and vertical wavenumber components are $k = \pm 2\pi/\lambda_x$ with $\lambda_x = 8$ km and $m = \pm 2\pi/\lambda_z$ with $\lambda_z = 4$ km, respectively. Red and blue contour lines refer to ± 0.95 times the wave amplitude and illustrate phase lines. The dashed black lines refer to the horizontal position where the vertical time series shown in Fig. 4 are recorded.

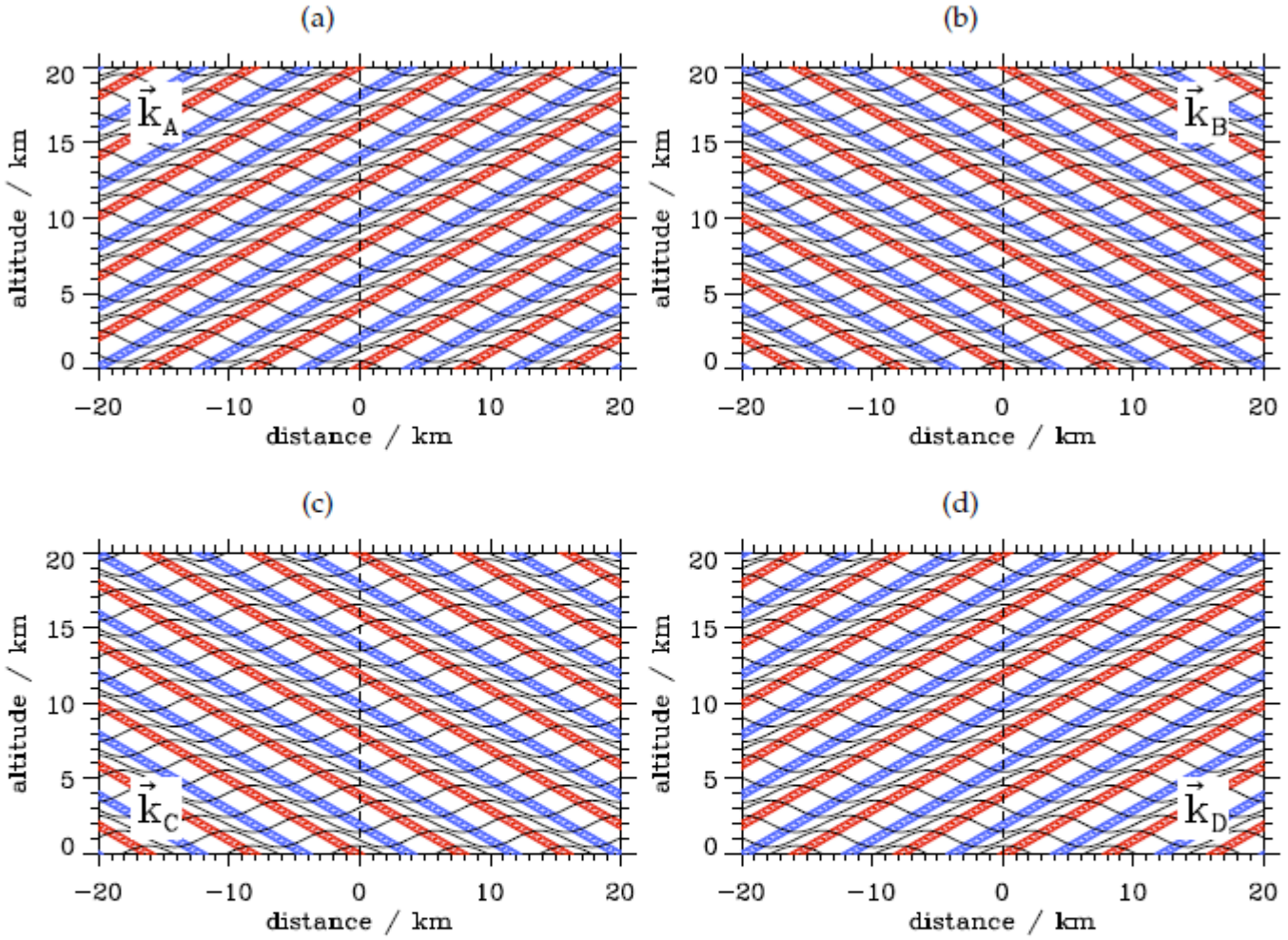

Figure 3. Spatial snapshots of the vertical displacements $\xi(x,z,t)$ of horizontally and vertically propagating plane waves for the four wavenumber vectors $\vec{k}_A$ (a), $\vec{k}_B$ (b), $\vec{k}_C$ (c), and $\vec{k}_D$ (d) at $t = 24$ min, respectively. The values of the horizontal and vertical wavenumber components are $k = \pm 2\pi/\lambda_x$ with $\lambda_x = 8$ km and $m = \pm 2\pi/\lambda_z$ with $\lambda_z = 4$ km, respectively. Red and blue contour lines refer to ± 0.95 times the wave amplitude and illustrate phase lines. The dashed black lines refer to the horizontal position where the vertical time series shown in Fig. 4 are recorded.

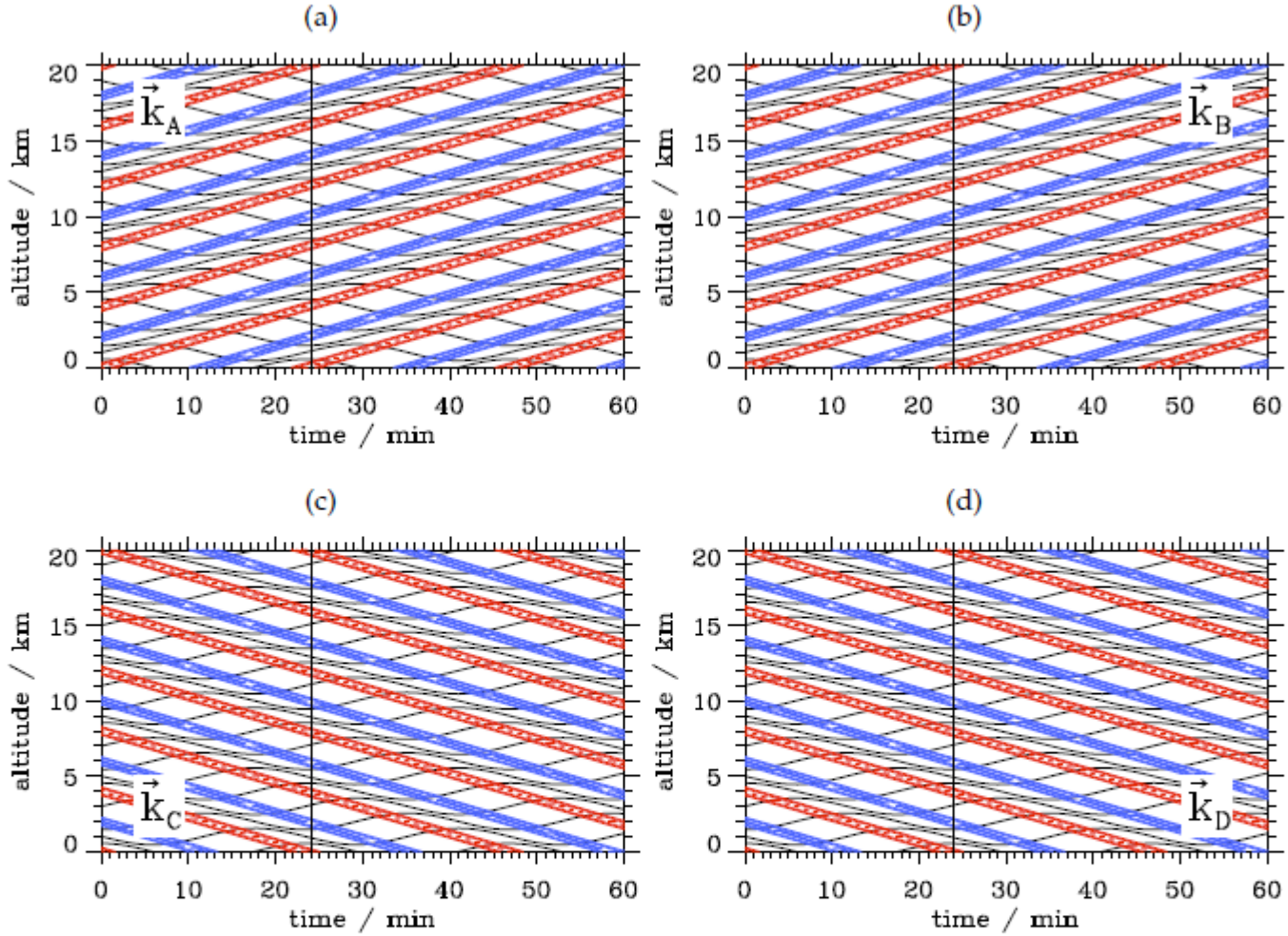

Figure 4. Vertical time series of the vertical displacements $\zeta(x,z,t)$ of horizontally and vertically propagating plane waves for the four wavenumber vectors $\vec{k}_A$ (a), $\vec{k}_B$ (b), $\vec{k}_C$ (c), and $\vec{k}_D$ (d) recorded at the positions marked in Fig. 3. The values of the horizontal and vertical wavenumber components are $k = \pm 2\pi/\lambda_x$ with $\lambda_x = 8$ km and $m = \pm 2\pi/\lambda_z$ with $\lambda_z = 4$ km, respectively. Red and blue contour lines refer to ± 0.95 times the wave amplitude and illustrate phase lines. The vertical black lines refer to the time when the plots shown in Fig. 3 are drawn.

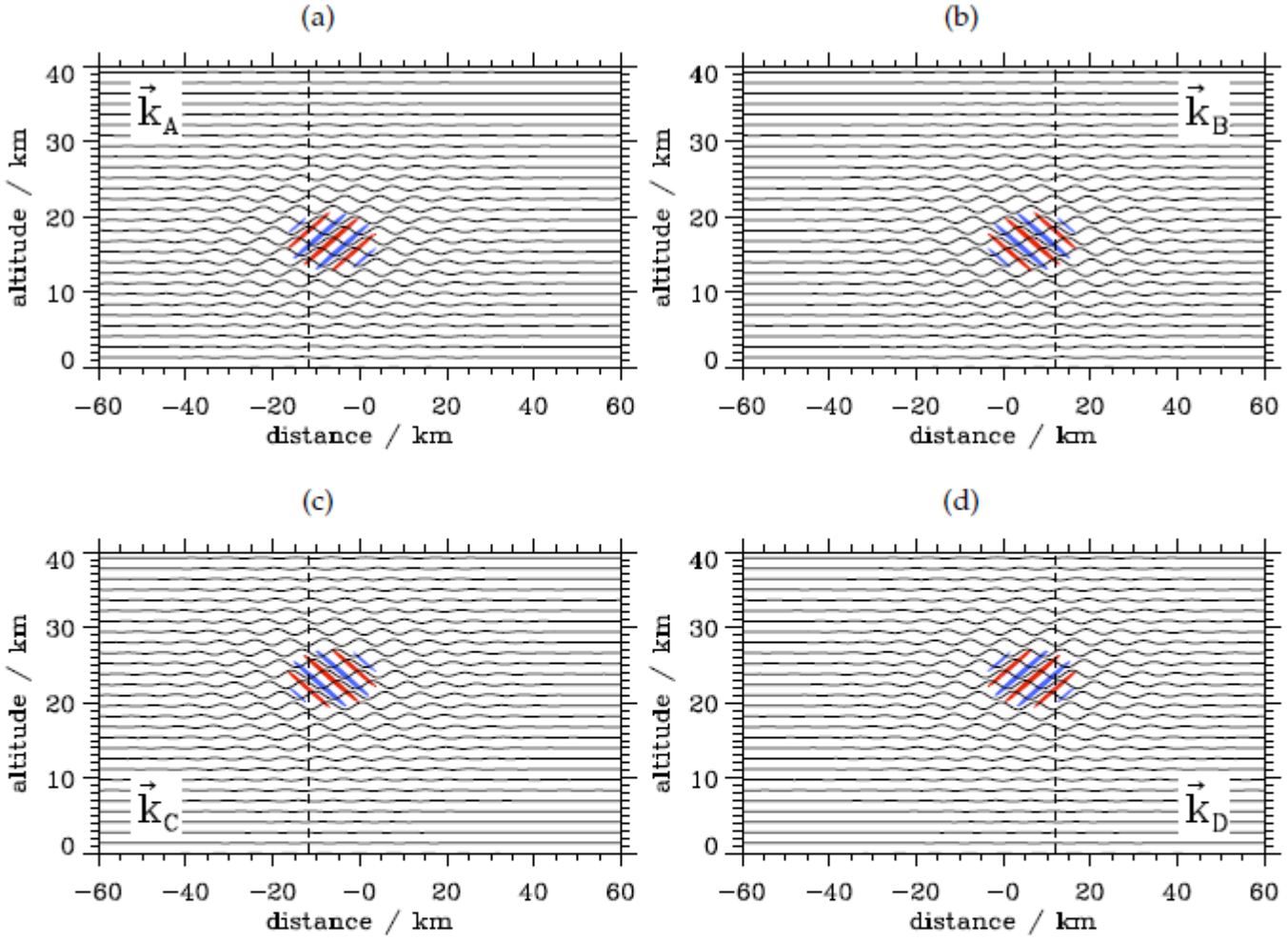

Figure 5. Spatial snapshots of the vertical displacements $\xi(x,z,t)$ of horizontally and vertically propagating wave packets with four different wavenumber vectors $\vec{k}_A$ (a), $\vec{k}_B$ (b), $\vec{k}_C$ (c), and $\vec{k}_D$ (d) at $t = 24$ min, respectively. The wave packets are propagating downward ($c_{gz} < 0$) in the top row and upward ($c_{gz} > 0$) in the bottom row. Red and blue contour lines refer to ± 0.95 times the wave amplitude and illustrate phase lines. The dashed black lines refer to the horizontal position where the time series shown in Fig. 6 are recorded.

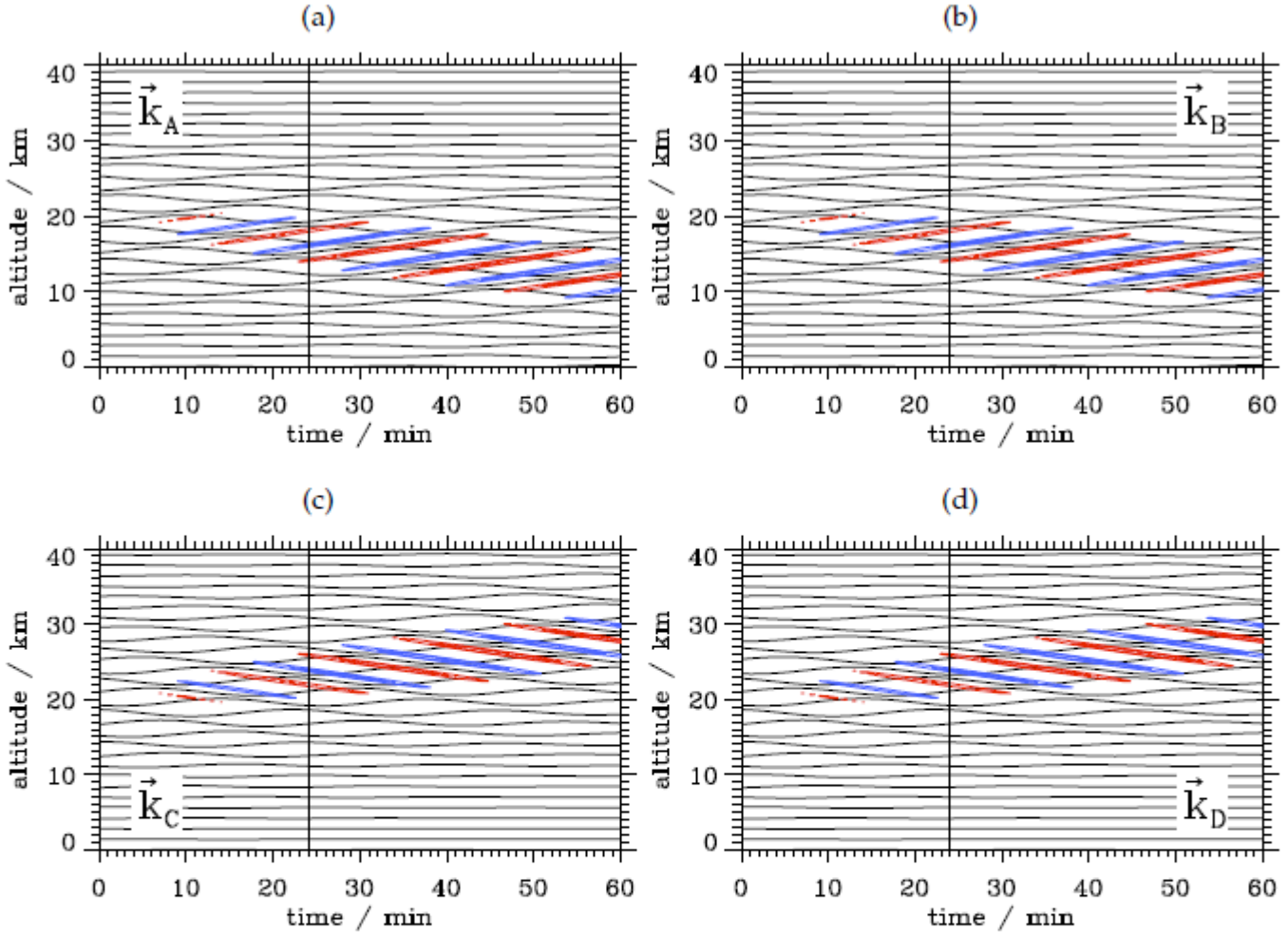

Figure 6. Vertical time series of the vertical displacements $\xi(x,z,t)$ of horizontally and vertically propagating wave packets with four different wavenumber vectors $\vec{k}_A$ (a), $\vec{k}_B$ (b), $\vec{k}_C$ (c), and $\vec{k}_D$ (d) recorded at the positions marked in Fig. 5, respectively. The wave packets are propagating downward ($c_{gz} < 0$) in the top row and upward ($c_{gz} > 0$) in the bottom row. Red and blue contour lines refer to ± 0.95 times the wave amplitude and illustrate phase lines. The vertical black lines refer to the time when the plots shown in Fig. 5 are drawn.

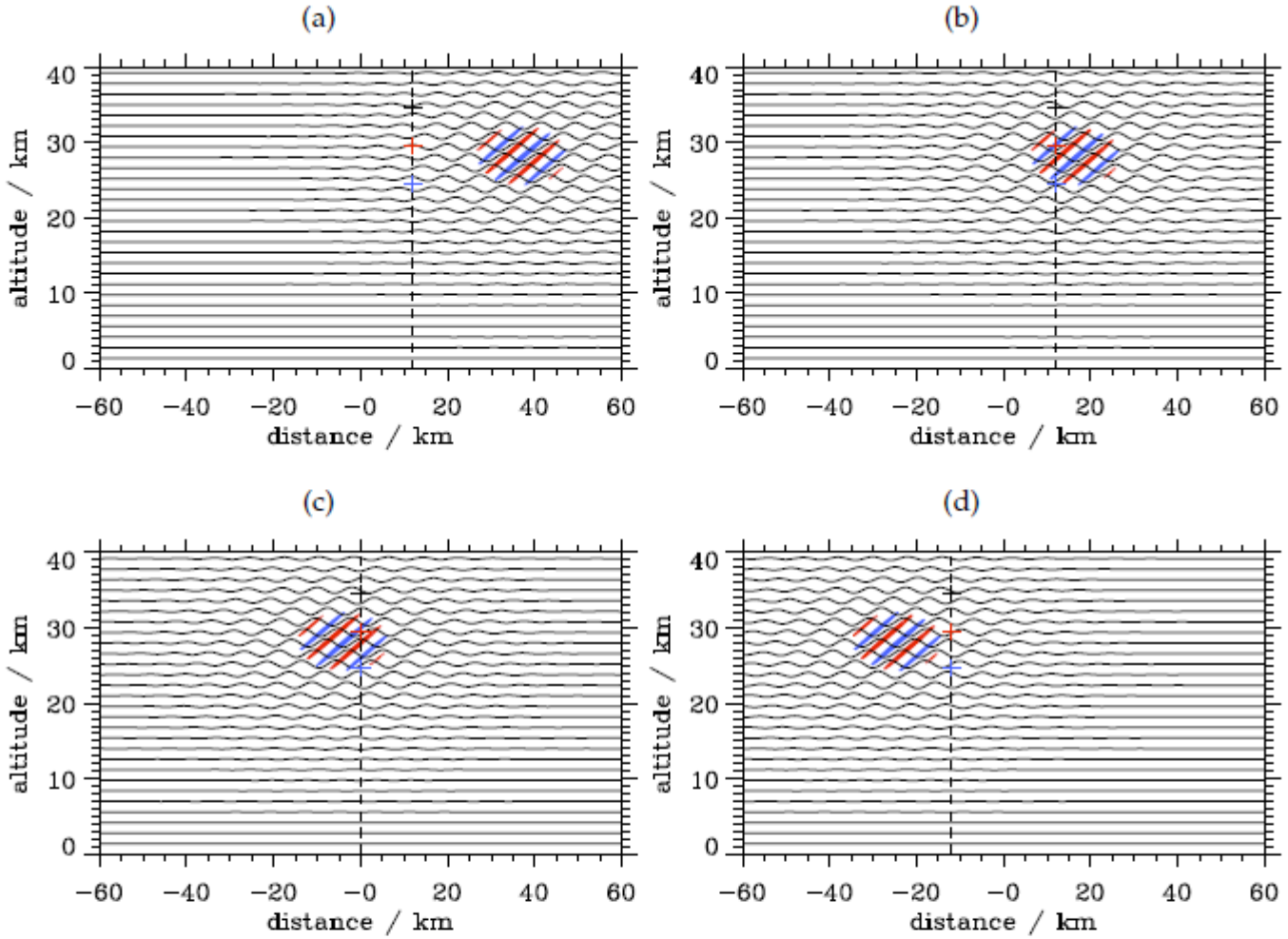

Figure 7. Spatial snapshots of the vertical displacements $\xi(x,z,t)$ of horizontally and vertically propagating wave packets with wavenumber vectors $\vec{\mathbf{k}}_D$ at $t = 60$ min. The wave frequencies are Doppler shifted by $U = +c_{px}$ (**a**), $U = 0$ (**b**), $U = -c_{px}$ (**c**), and $U = -2\,c_{px}$ (**d**), respectively. Red and blue contour lines refer to ± 0.95 times the wave amplitude and illustrate phase lines. The dashed vertical black lines refer to the horizontal positions $x = -12$ km, 0, 12 km where the vertical time series shown in Fig. 8 are recorded. The blue, red, and black crosses refer to the vertical positions $z = 24.6$ km, 29.6 km, and 34.6 km where the time series of Fig. 9 are recorded.

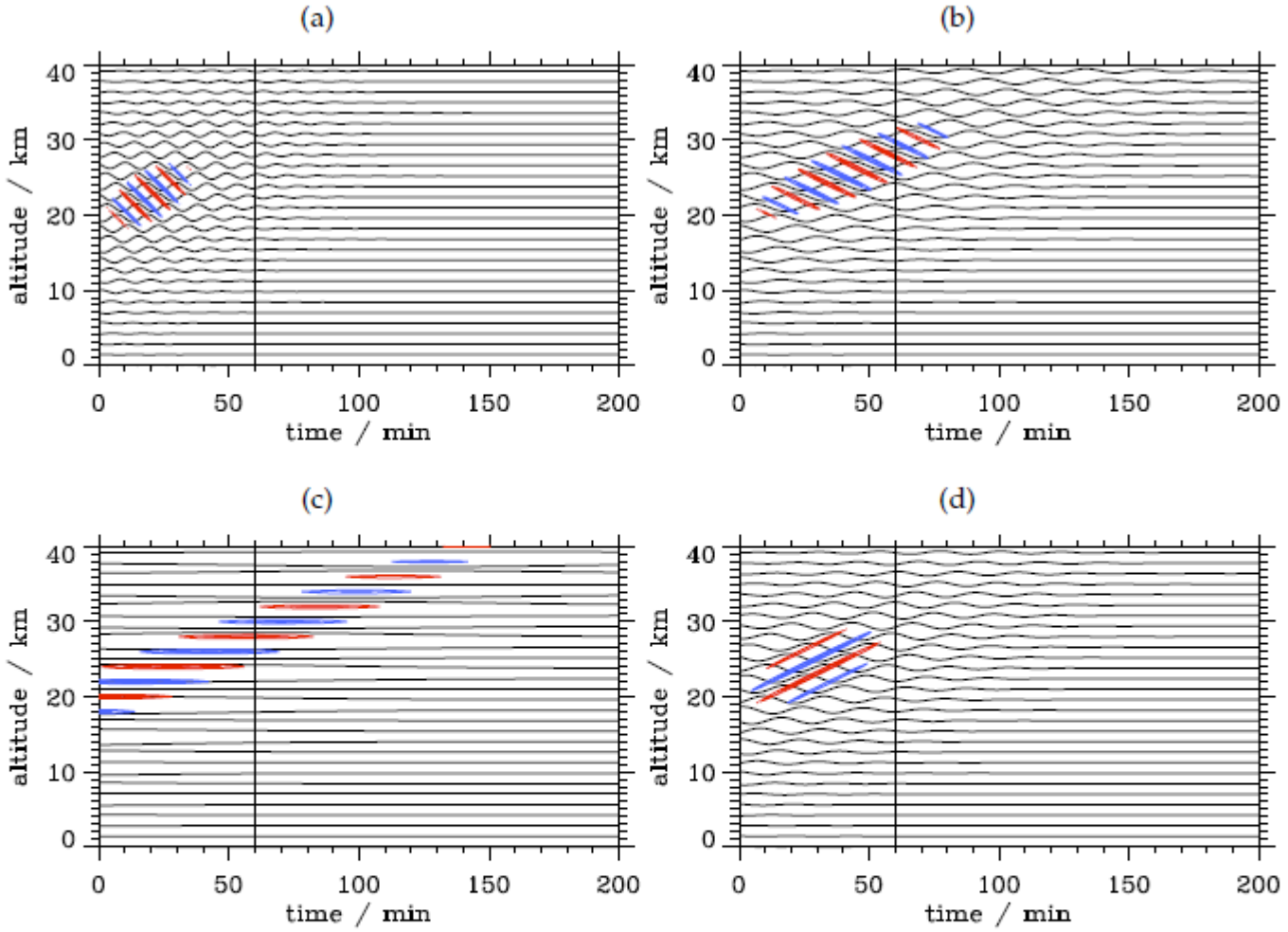

Figure 8. Vertical time series of the vertical displacements $\xi(x,z,t)$ of horizontally and vertically propagating wave packets with the wavenumber vector $\vec{k}_D$ recorded at the horizontal positions marked in Fig. 7. The wave frequencies are Doppler shifted by $U=+c_{Px}$ (**a**), $U=0$ (**b**), $U=-c_{Px}$ (**c**), and $U=-2\,c_{Px}$ (**d**), respectively. Red and blue contour lines refer to ± 0.95 times the wave amplitude and illustrate phase lines.The vertical black lines refer to the time $t=60$ min where the altitude-distance plots are shown in Fig. 7.

non-hydrostatic

hydrostatic, nonrotating

hydrostatic, rotating

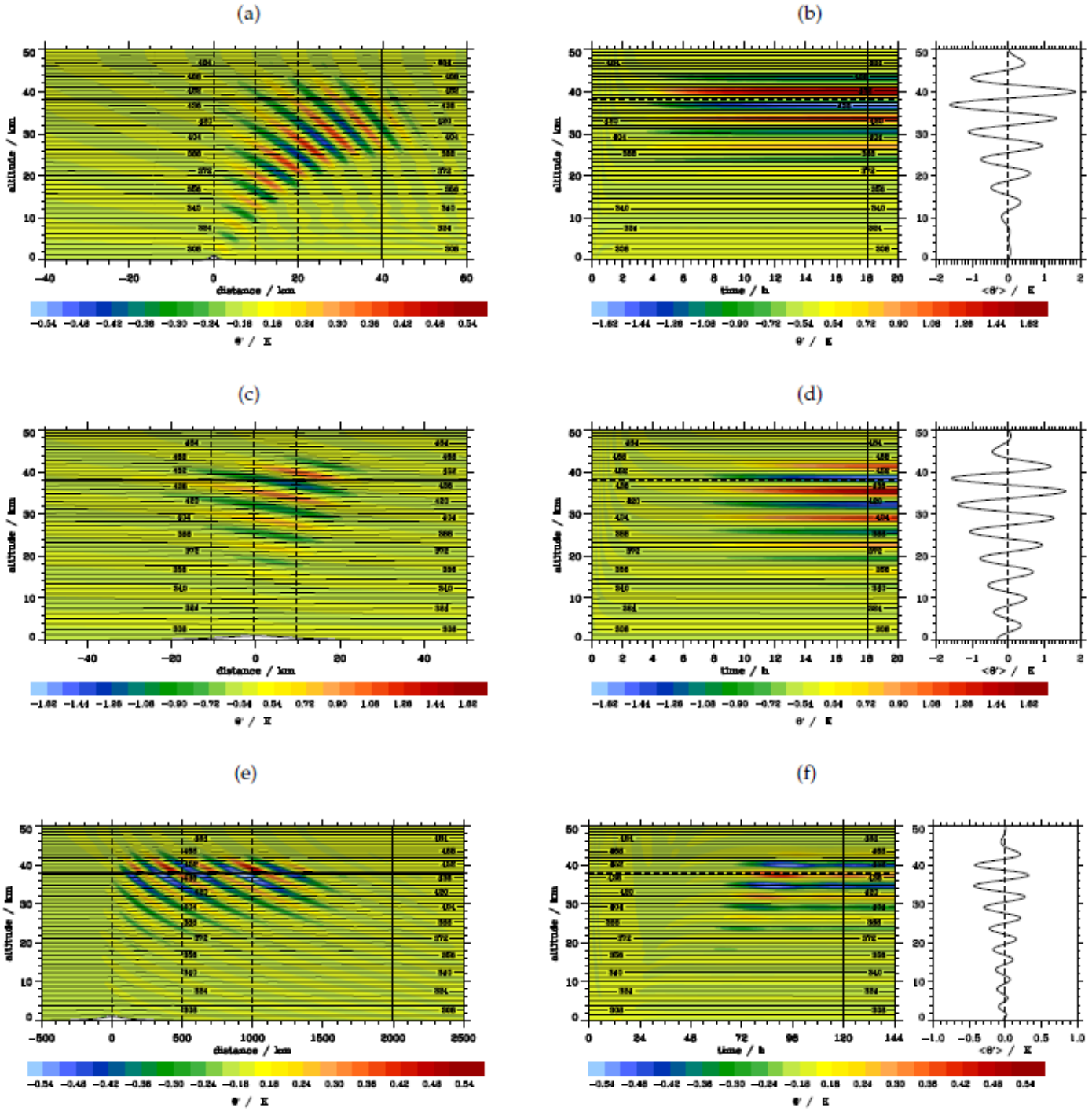

Comparison ECMWF Rayleigh Lidar

Benedikt Ehard (part of PhD Thesis)

Collaboration ECMWF (Nils Wedi, Sylvie Malardel)

Task Force: Stratosphere (Ted Shepard)

Vertical resolution and model levels of the IFS

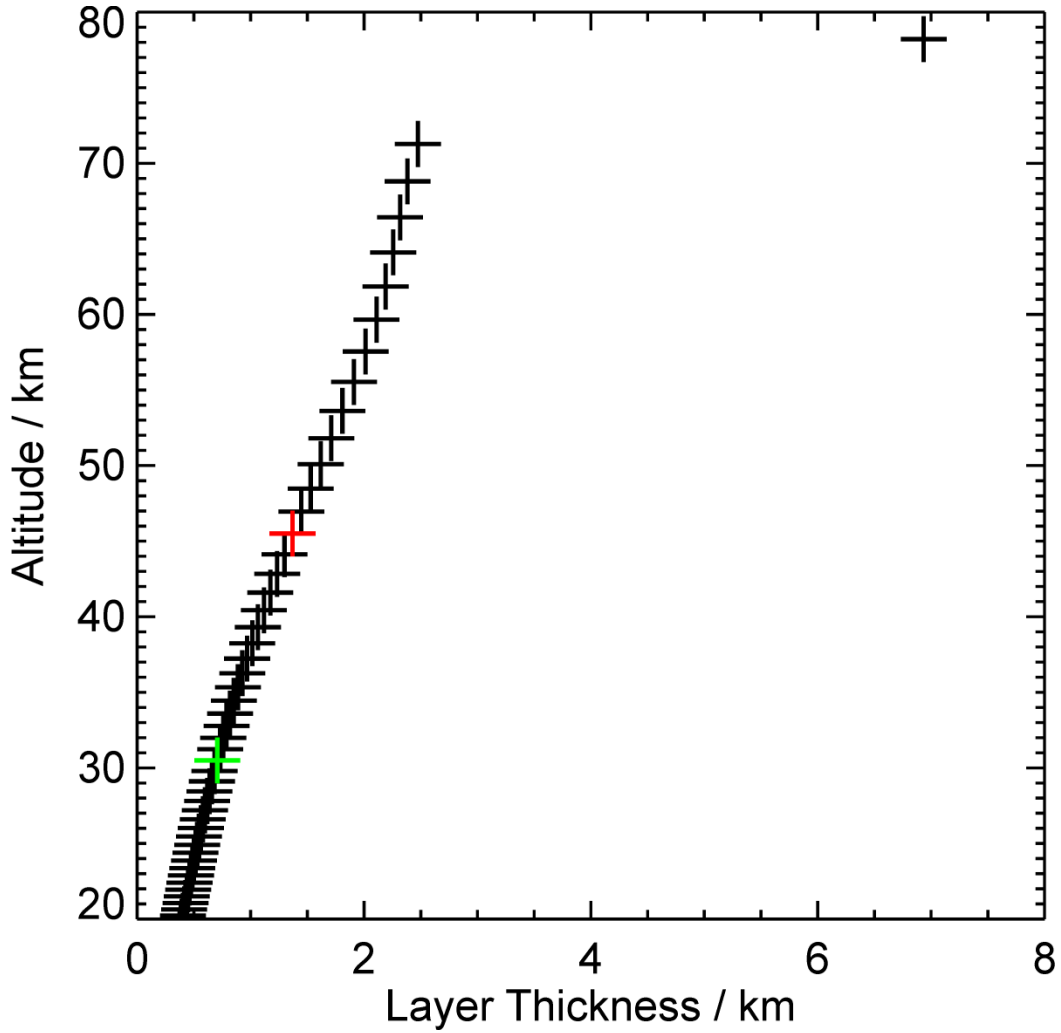

Level 15: „hard sponge“

Level 30: „weak sponge“

The IFS cycle 40r1 at Lauder, New Zealand

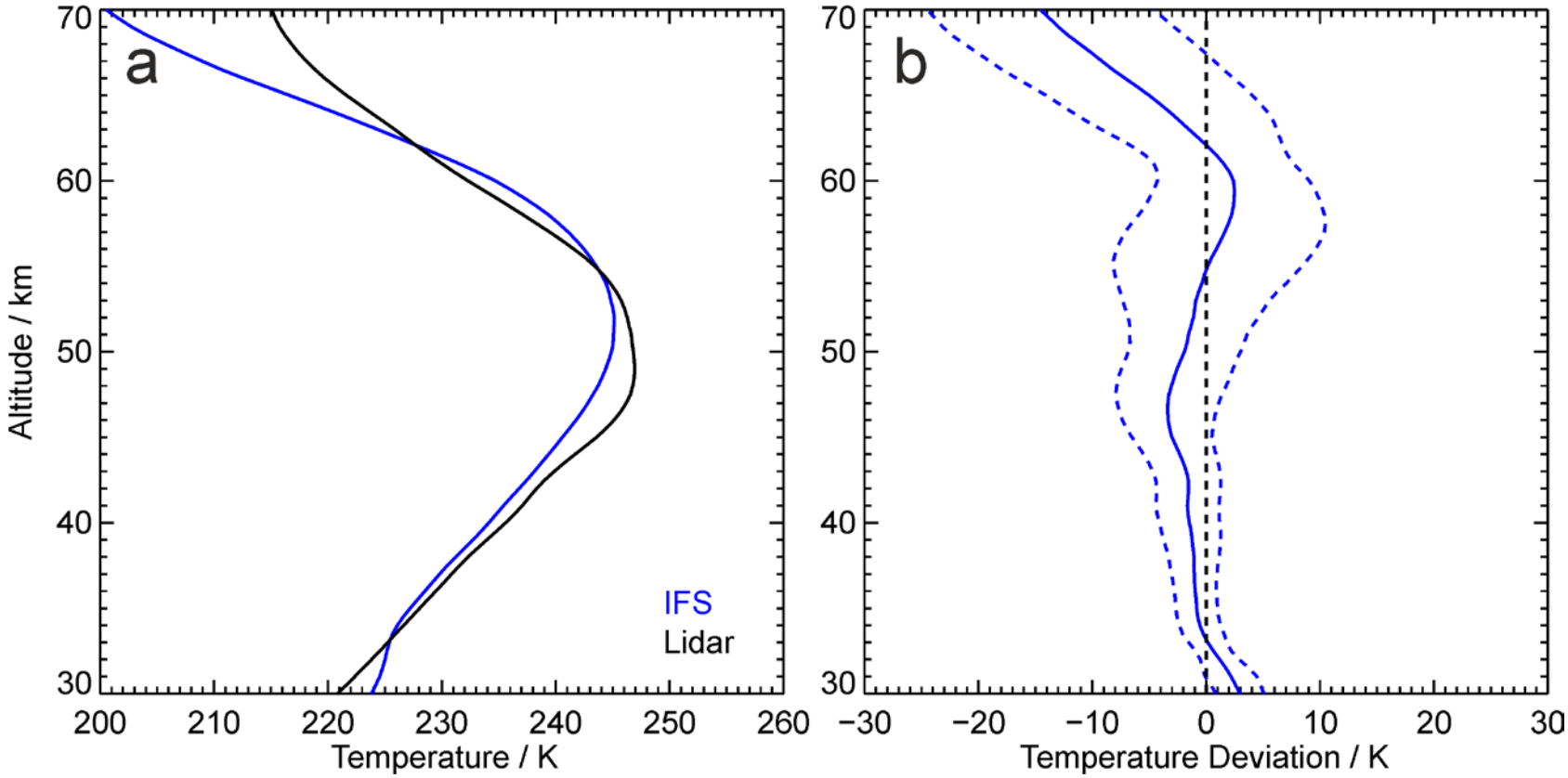

Capability of resolving gravity waves by the IFS above Lauder (1 August 2014)

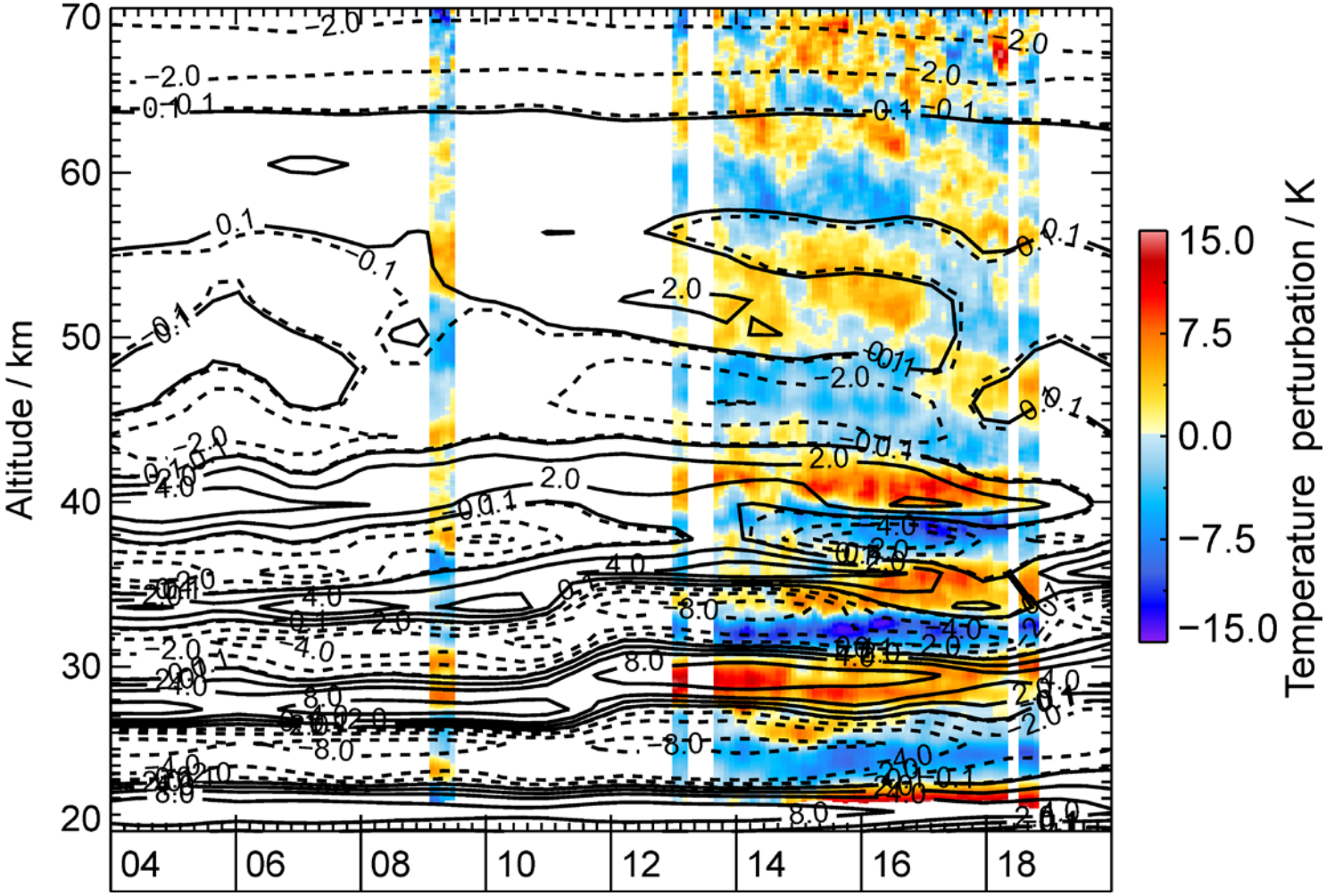

Comparing temperature perturbations from July to September 2014 above Lauder

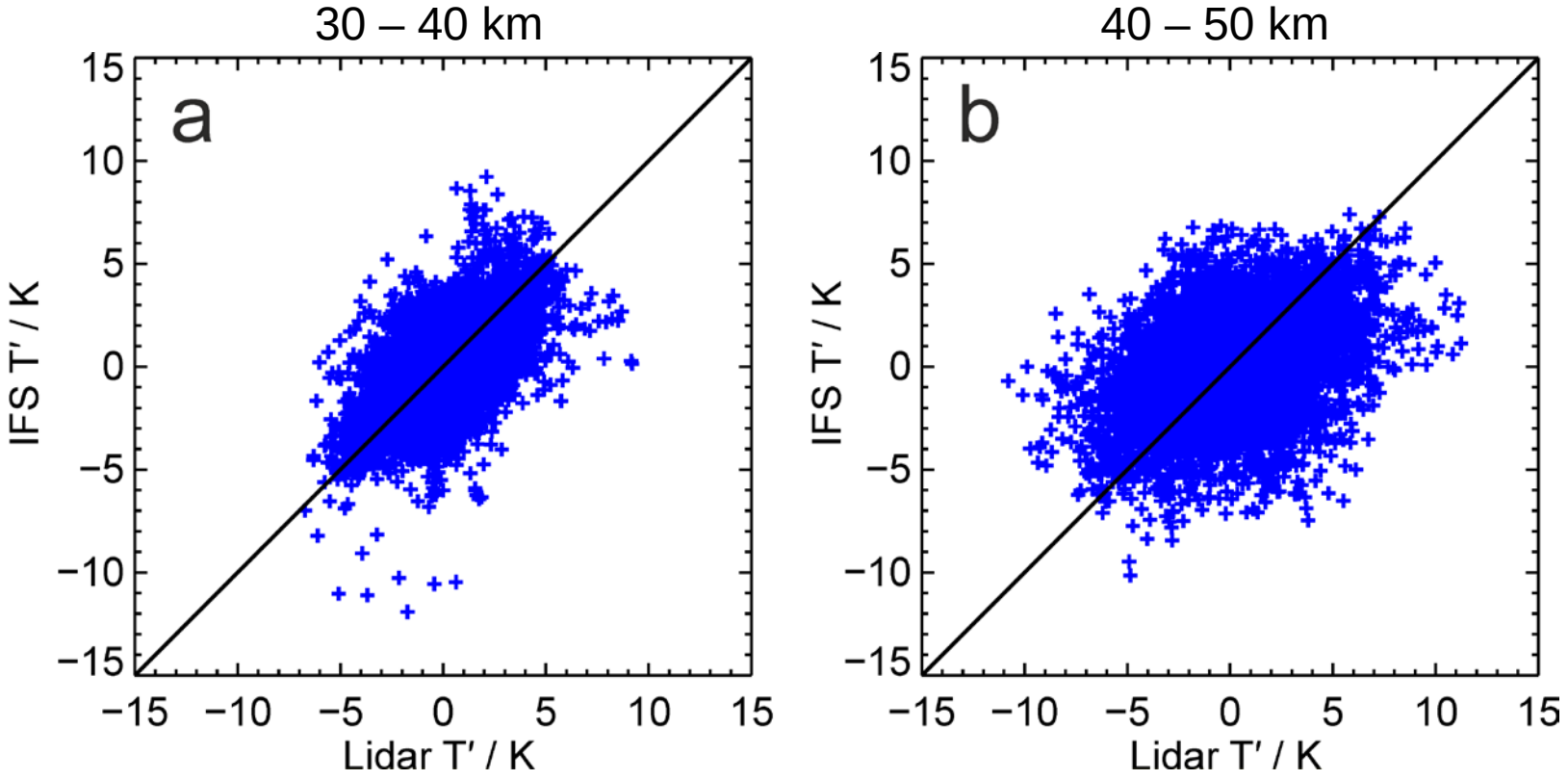

Correlation: 0.57

Correlation: 0.39

Better horizontal resolution of the IFS (16 km vs 9 km)

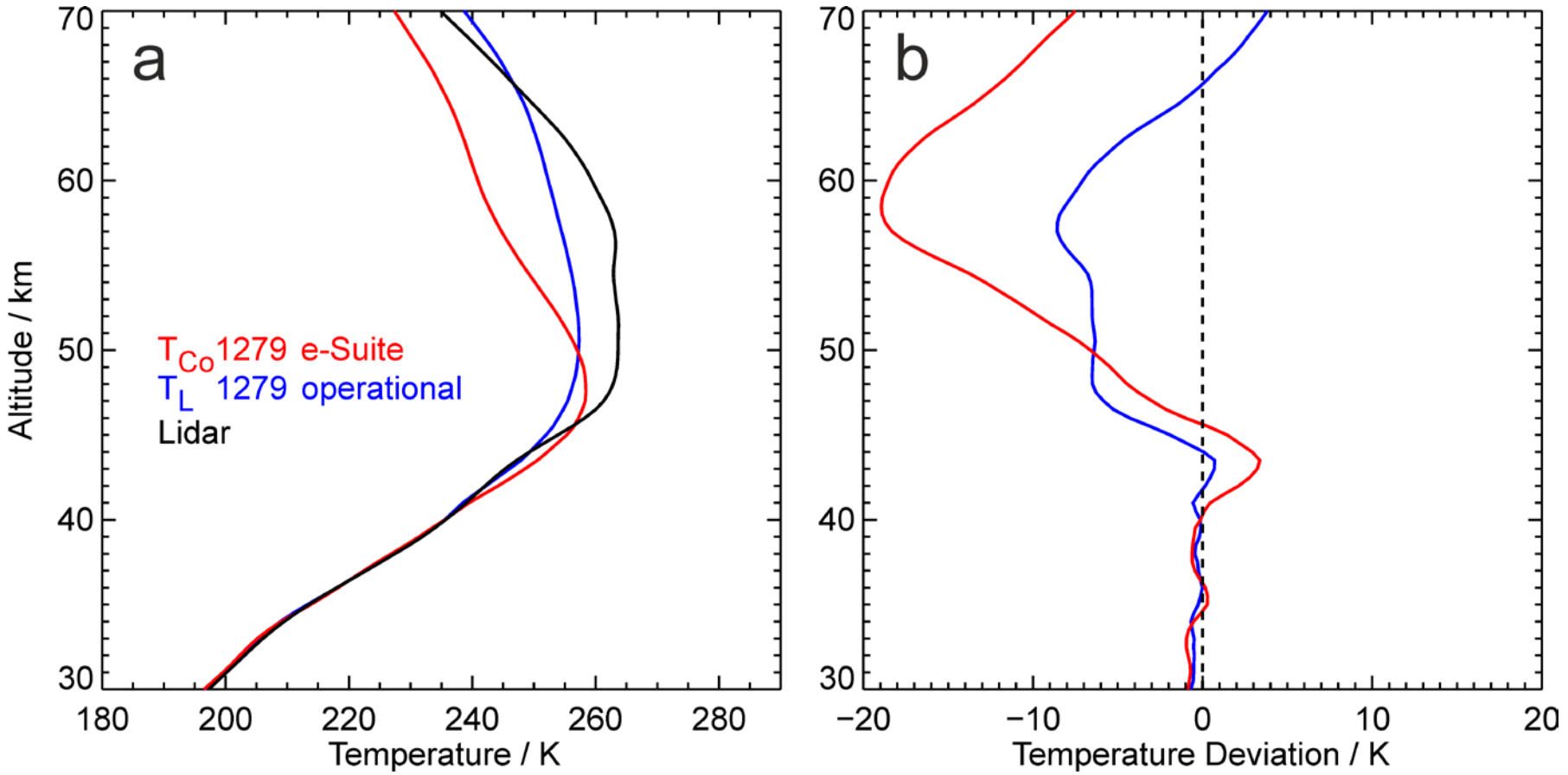

Ongoing Work

Case Study 4th July RF16 (Martina Bramberger)

RF25 (Tanja Portele, Andreas Dörnbrack)

Radiosonde Analysis (Sonja Gisinger)